Cell

Delineating the conformational landscape of the adenosine A_{2A} receptor during G protein coupling

Graphical abstract

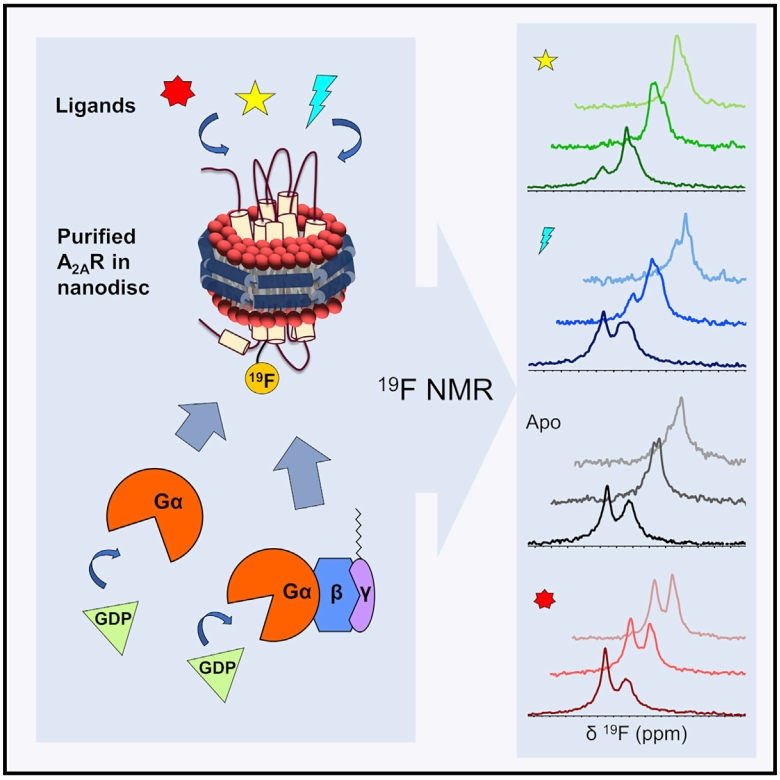

Highlights

- ^{19}F NMR of the A_{2A} receptor reveals a conformational ensemble in lipid bilayers
- Binding of G protein stabilizes a precoupled activation intermediate
- Two distinct active states facilitate nucleotide exchange by full or partial agonist
- Gβγ is key in facilitating allosteric signal transmission within the ternary complex

Authors

Shuya Kate Huang, Aditya Pandey, Duy Phuoc Tran, ..., Roger K. Sunahara, Adnan Sljoka, R. Scott Prosser

Correspondence

adnan.sljoka@riken.jp (A.S.), scott.prosser@utoronto.ca (R.S.P.)

In brief

Monitoring conformational ensembles of a GPCR along the entire activation pathway in lipid bilayer captures key receptor states associated with G protein coupling and uncovers the role of Gβγ in facilitating ligand-dependent allosteric signal transmission.

Huang et al., 2021, Cell *184*, 1884–1894
April 1, 2021
https://doi.org/10.1016/j.cell.2021.02.041

CellPress

Cell

Article

Delineating the conformational landscape of the adenosine A_{2A} receptor during G protein coupling

Shuya Kate Huang,[1] Aditya Pandey,[1,2] Duy Phuoc Tran,[3] Nicolas L. Villanueva,[4] Akio Kitao,[3] Roger K. Sunahara,[4] Adnan Sljoka,[1,5,*] and R. Scott Prosser[1,2,6,*]

[1]Department of Chemistry, University of Toronto, UTM, 3359 Mississauga Road North, Mississauga, Ontario L5L 1C6, Canada
[2]Department of Biochemistry, University of Toronto, 1 King's College Circle, Toronto, Ontario M5S 1A8, Canada
[3]School of Life Science and Technology, Tokyo Institute of Technology, 2-12-1 Ookayama, Meguro-ku, Tokyo 152-8550, Japan
[4]Department of Pharmacology, University of California San Diego School of Medicine, 9500 Gilman Drive, La Jolla, CA 92093, USA
[5]RIKEN Center for Advanced Intelligence Project, RIKEN, 1-4-1 Nihombashi, Chuo-ku, Tokyo 103-0027, Japan
[6]Lead contact
*Correspondence: adnan.sljoka@riken.jp (A.S.), scott.prosser@utoronto.ca (R.S.P.)
https://doi.org/10.1016/j.cell.2021.02.041

SUMMARY

G-protein-coupled receptors (GPCRs) represent a ubiquitous membrane protein family and are important drug targets. Their diverse signaling pathways are driven by complex pharmacology arising from a conformational ensemble rarely captured by structural methods. Here, fluorine nuclear magnetic resonance spectroscopy (^{19}F NMR) is used to delineate key functional states of the adenosine A_{2A} receptor ($A_{2A}R$) complexed with heterotrimeric G protein ($G\alpha_s\beta_1\gamma_2$) in a phospholipid membrane milieu. Analysis of $A_{2A}R$ spectra as a function of ligand, G protein, and nucleotide identifies an ensemble represented by inactive states, a G-protein-bound activation intermediate, and distinct nucleotide-free states associated with either partial- or full-agonist-driven activation. The $G\beta\gamma$ subunit is found to be critical in facilitating ligand-dependent allosteric transmission, as shown by ^{19}F NMR, biochemical, and computational studies. The results provide a mechanistic basis for understanding basal signaling, efficacy, precoupling, and allostery in GPCRs.

INTRODUCTION

One-third of current pharmaceuticals target G-protein-coupled receptors (GPCRs) (Hauser et al., 2017), the largest family of membrane proteins in the human genome and mediators of diverse biological processes through signal transduction across the cell membrane. The adenosine A_{2A} receptor ($A_{2A}R$) is a prototypical class A GPCR and a target for the treatment of respiratory and cardiovascular diseases (Guerrero, 2018), inflammation and cancer (Effendi et al., 2020; de Lera Ruiz et al., 2014; Yu et al., 2020), and diseases of the central nervous system (Zheng et al., 2019). Upon activation, $A_{2A}R$ engages the heterotrimeric stimulatory G protein $G_s\alpha\beta\gamma$, resulting in nucleotide exchange, dissociation of the α and $\beta\gamma$ subunits, and downstream activation of effector proteins. This theme is repeated in sensory signaling (vision, taste, smell, pain), neurotransmission, cardiovascular function, and immune response in over 800 other GPCRs (Fredriksson et al., 2003). The recent renaissance in X-ray crystallography and cryoelectron microscopy (cryo-EM) has generated high-resolution structures of many GPCRs, including $A_{2A}R$, in both their inactive states and G-protein-complexed active states (Carpenter et al., 2016; García-Nafría et al., 2018; Liu et al., 2012; Weis and Kobilka, 2018). This has spurred structure-based drug design (Congreve et al., 2020) and provided a greater understanding of the mechanism of activation.

Solution-state nuclear magnetic resonance (NMR) spectroscopy builds upon static crystallography and cryo-EM by capturing the entire conformational ensemble, using native constructs under physiological conditions. If the representative states are sufficiently resolved, relaxation experiments can provide additional insights into dynamics and lifetimes of states spanning nanoseconds to seconds. Many groups have taken the approach of isotopic labeling for one- or two-dimensional NMR of GPCRs in detergent micelles (Clark et al., 2017; Eddy et al., 2018; Frei et al., 2020; Isogai et al., 2016; Manglik et al., 2015; Nygaard et al., 2013; Solt et al., 2017; Sounier et al., 2015; Wu et al., 2020; Ye et al., 2016) and model membrane systems (Casiraghi et al., 2016; Kofuku et al., 2014). These studies, along with single-molecule fluorescence spectroscopy (Bockenhauer et al., 2011; Gregorio et al., 2017), electron paramagnetic resonance spectroscopy (Van Eps et al., 2017), and molecular dynamics (MD) simulations (Dror et al., 2011; Provasi et al., 2011), suggest that activation proceeds through complex allosteric pathways and multiple intermediate states. However, it is difficult to interpret the observed "active" states unless they can be measured in the presence of the heterotrimeric G protein.

The series of steps during activation (i.e., G protein binding, nucleotide exchange, and dissociation of the subunits) may all be a consequence of specific states within the active ensemble, which can be further complicated by the effects of the orthosteric ligand. Resolving the active ensemble, therefore, is key to understanding the mechanism of activation in both the receptor and the G protein.

Here, we use NMR to resolve the conformational ensemble of $A_{2A}R$, free of any stabilizing mutations, reconstituted in lipid bilayers and complexed to the full-length heterotrimeric G protein. Fluorine (^{19}F) NMR is a particularly sensitive technique to electrostatic and van der Waals environments and exhibits a large chemical shift dispersion, enabling improved resolution of states (Ye et al., 2015). Critically, as a one-dimensional method, potentially dynamic states that manifest as broad lines are also resolvable and quantifiable, whereas their observation might be obscured by multidimensional NMR methods that are susceptible to relaxation during insensitive nuclei enhancement by polarization transfer (INEPT) times (Cavanagh et al., 2007). Previous ^{19}F NMR studies of $A_{2A}R$ in detergent micelles (Ye et al., 2016, 2018) identified two inactive-state conformers in fast exchange and two active-like conformers stabilized by partial or full agonists, respectively. Using the same construct ($A_{2A}R$ (2–317) with a single cysteine mutation, V229C, for ^{19}F-labeling on transmembrane helix 6 [TM6]), the current work examines receptor states associated with G protein coupling and nucleotide exchange in discoidal phospholipid-containing reconstituted high-density-lipoprotein particles (rHDLs, commonly known as nanodiscs) and in the presence of the stimulatory heterotrimeric G protein (composed of human $G_s\alpha$-short, β_1, and γ_2, henceforth referred to as $G_s\alpha\beta\gamma$ or $G\alpha\beta\gamma$) (Figures S1 and S2). By recording $A_{2A}R$ spectra as a function of orthosteric ligand, G protein, and nucleotide, the representative states in the ensemble can be monitored along the entire activation pathway—capturing signatures of both precoupling and nucleotide release. We discovered that the $G\beta\gamma$ subunit not only anchors $G\alpha$ to the membrane but also is critical in transducing ligand efficacy. Through biochemical, biophysical, and computational methods, we seek to connect the observed conformational states and allosteric pathways of a receptor to the downstream pharmacological effects of basal signaling and partial agonism. Building upon previously published work on dynamical aspects of GPCRs, this study enables a more complete characterization of the signaling process through heterotrimeric G proteins and provides a basis for understanding receptor pharmacology from an ensemble perspective.

RESULTS AND DISCUSSION

$A_{2A}R$ adopts a precoupled activation intermediate and two distinct active states that mediate nucleotide exchange

The classical view of GPCR activation involves an equilibrium between an inactive (R) and an active (R*) pose (Park et al., 2008). The agonist induces an allosteric response, shifting the receptor population to the R* state to enable binding and coupling to the G protein. This idea is recapitulated in the cubic ternary complex model (Weiss et al., 1996) that encompasses precoupling, a phenomenon wherein the receptor-G protein complex is assembled prior to activation by ligands (Neubig, 1994; Rebois and Hébert, 2003).

^{19}F NMR provides a more detailed perspective of the R-R* transition, wherein inactive and active signatures of $A_{2A}R$ can be resolved as a function of ligands and $G\alpha$ (Figure 1). The spectra not only reveal a clear pattern of activation featuring a population shift to the active ensemble but also reveal subtleties regarding the conformational ensemble that imply a more complex response. For example, the resonance associated with the inactive pose not only decreases in population but also shifts downfield in response to activating conditions. This is likely a consequence of conformational exchange between two inactive conformers in which a salt bridge (also known as ionic lock) between $R102^{3.50}$ of the highly conserved E(D)RY motif on TM3 and $E228^{6.30}$ on TM6 is either intact or broken. Here, superscripts denote the Ballesteros-Weinstein numbering for GPCRs (Ballesteros and Weinstein, 1995). This ionic lock motif stabilizes the inactive state of many class A receptors (Ballesteros et al., 2001; Vogel et al., 2008). In $A_{2A}R$, both the ionic lock "on" and "off" conformers are part of the inactive ensemble, and higher efficacy ligands shift this equilibrium toward the ionic lock "off" state (Doré et al., 2011). Interestingly, the inactive state chemical shift of the inverse agonist saturated receptor is nearly coincident with those of apo (ligand-free)-$A_{2A}R$, implying an unchanged ionic lock equilibrium between the two conditions. In the case of the partial agonist, there is a subtle inflection point in the inactive state resonance that aligns with the ionic lock "off" state. This suggests that the two conformers are in relatively slow exchange ($k_{ex} \leq \sim 400\ s^{-1}$) in lipid bilayers. By contrast, prior studies of β_2AR and $A_{2A}R$ in detergent micelles suggested that ionic lock fluctuations occurred on a relatively fast NMR timescale (Manglik et al., 2015; Ye et al., 2016).

Closer inspection of the spectral series in Figure 1 reveals that active pose is also represented by multiple states. Here, two distinct resonances, at −61.7 and −61.9 ppm, were stabilized by the addition of either agonist (Figure 1A) or partial agonist in the presence of $G\alpha$ (Figure 1B). These effects are more pronounced upon removal of guanosine diphosphate (GDP) by apyrase. In the absence of an orthosteric ligand (Figure 1C), addition of $G\alpha$ resulted in modest change. The results show that even under basal conditions, the receptor samples multiple active-like states including those that facilitate GDP release. The propensity for establishing a particular conformer is influenced by ligands and $G\alpha$ while the same basis set of states are observed across a range of conditions, suggesting that conformational selection plays a significant role in receptor activation.

The overlap among resonances in the active ensemble poses challenges to robust spectral deconvolutions since nothing *a priori* is known of the respective line widths. An attempt to deconvolve the ^{19}F NMR spectrum in the presence of the full agonist 5′-*N*-ethylcarboxamidoadenosine (NECA) is shown in Figure S3. In the absence of transverse relaxation time (T_2) measurements, it is sufficient to obtain a fitted spectrum closely matching the experimental result by considering one inactive state (peak 1) and two active-like states (peaks 2 and 3). However, T_2 relaxation measurements predict significantly narrower line widths for peaks 1 and 3. The observed broadening of

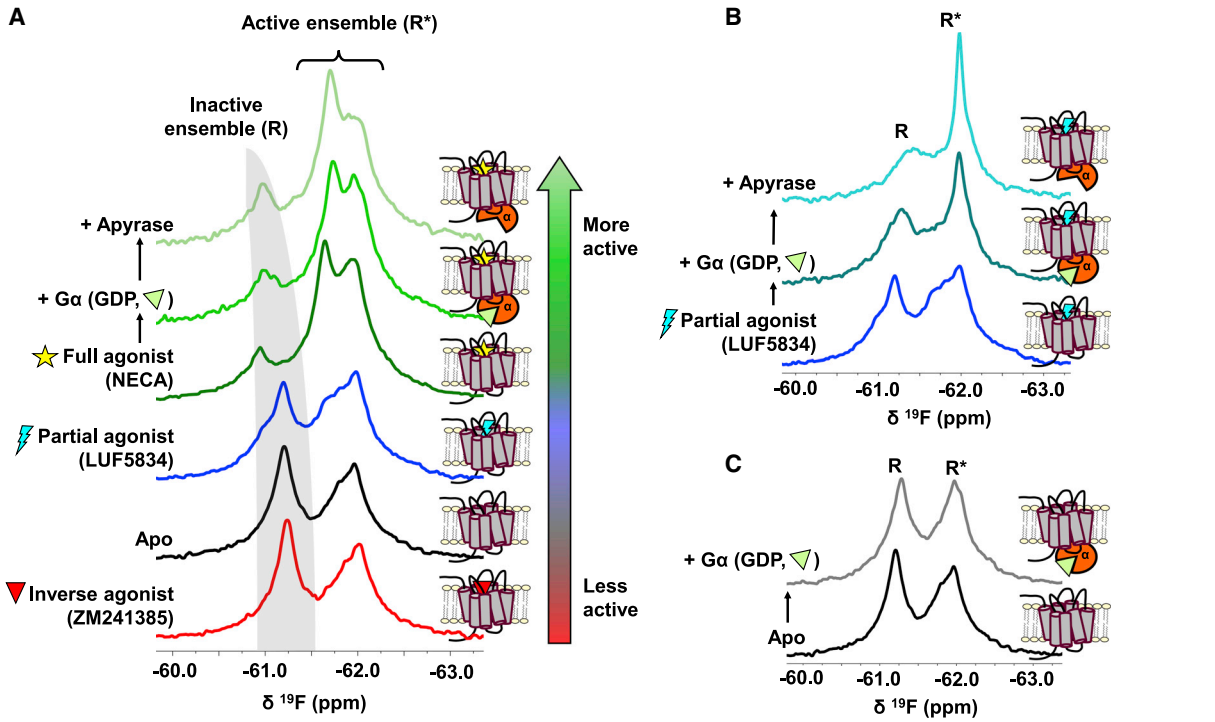

Figure 1. $A_{2A}R$ adopts an ensemble of conformational states and an activation mechanism consistent with conformational selection

(A) ^{19}F NMR spectra of nanodisc-reconstituted $A_{2A}R$-V229C as a function of ligand, Gα, and nucleotide. Addition of apyrase removes nucleotide (GDP) from G proteins. The receptor was placed under increasingly activating conditions, as indicated by the color gradient bar. The apo receptor (black trace) samples both inactive (R, gray band) and active (R*) states, whose populations are modulated through the binding of ligands (antagonist, partial agonist, and full agonist), Gα, and GDP, in a lipid environment.

(B and C) Spectra of partial agonist-bound (B) or apo (C) receptor with and without Gα.

peak 1 is likely a consequence of slow (millisecond) exchange between two inactive-state signatures, discussed above. Similarly, inhomogeneous broadening in the vicinity of peak 3 must arise from one or more additional nearby resonances, indicating that the active ensemble as a whole consists of at least three distinct and interconverting conformations. This is in contrast to ^{19}F NMR spectra of $A_{2A}R$ reconstituted in detergent micelles, which gives rise to two active-state conformers (referred to as S_3 and $S_{3'}$ in our previous work) and an inactive ensemble with faster exchange dynamics (Ye et al., 2016). The lipid-stabilized receptors display slower exchange dynamics, a higher fraction of inactive states, and an overall improved spectral resolution (Figure 2).

The presence of the G protein heterotrimer is critical for both the assignment of functional states and understanding their role in facilitating signaling, as shown in Figure 3. Generally, the addition of $G_s\alpha\beta\gamma$-GDP shifts the receptor equilibrium to a predominantly active ensemble. However, the inactive fraction persists in the presence of the inverse agonist ZM241385, whose chemical shift is upfield (ionic lock "on") from that observed for the full-agonist-bound receptor (Figure 3A). This is consistent with the inverse agonist stabilizing the ionic lock "on" equilibrium, resulting in a reduced affinity to G protein and transitions to the active ensemble. Interestingly, the addition of $G_s\alpha\beta\gamma$ to the inverse- and partial-agonist-bound receptor results in an upfield shift of the inactive state. This is likely a result of millisecond timescale averaging between inactive and active conformers, which would contribute to line broadening and coalescence of the respective signatures. Furthermore, the addition of GDP-saturated $G_s\alpha\beta\gamma$ is generally accompanied by line broadening of the active states, particularly in the case of partial-and full-agonist-stabilized receptors. We interpret this as evidence of intermediate timescale exchange between conformers representing the active ensemble.

A global analysis of the NMR spectra suggests that the active ensemble encompasses at least three distinct states, designated A_1, A_2, and A_3 (spectral assignment details provided in STAR Methods). For the apo receptor (Figure 3B), addition of GDP-bound $G_s\alpha\beta\gamma$ dramatically shifts the equilibrium toward A_3, a change that is recapitulated in the inverse-agonist-bound (Figure 3A), partial-agonist-bound (Figure 3C), and full-agonist-bound (Figure 3D) spectra. We attribute A_3 to a precoupled conformation, which is likely responsible for the initial recognition between receptor and G protein. Precoupling has previously been shown for $A_{2A}R$ and other GPCRs (Braun and Levitzki, 1979; Galés et al., 2006; Nanoff and Stiles, 1993; Nobles et al., 2005) in addition to work supporting a G-protein-bound intermediate prior to formation of the high-affinity complex associated with GDP release (Dror et al., 2011; Du et al., 2019; Lee et al., 2019; Liu et al., 2019; Sounier et al., 2015). The current NMR spectra corroborate these findings while at the same time revealing the response of the entire conformational ensemble

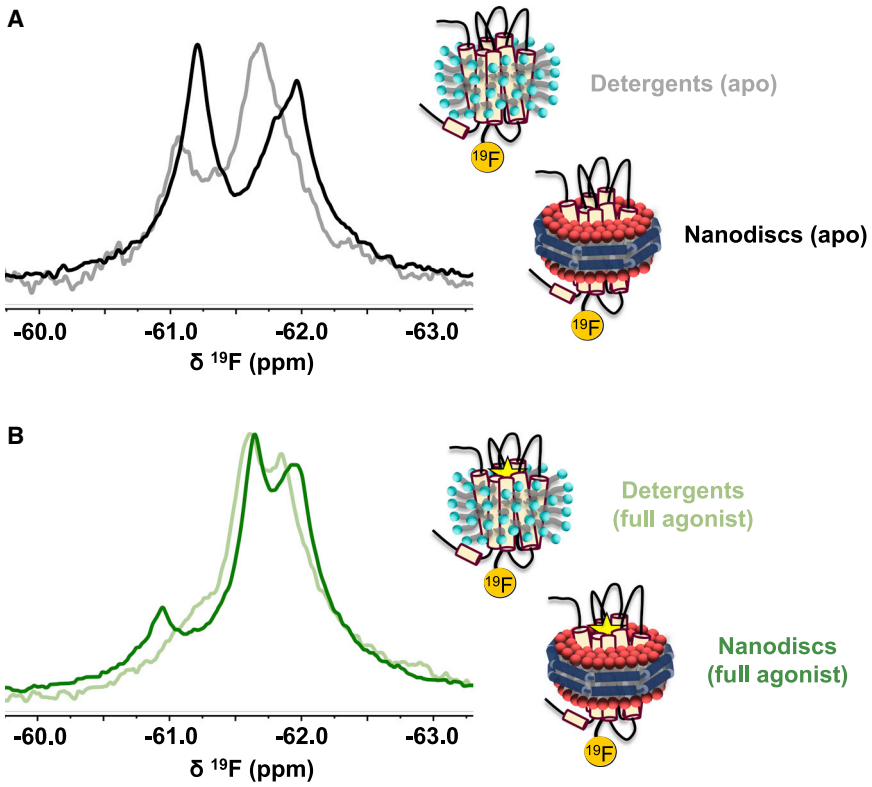

Figure 2. $A_{2A}R$ exhibits a different distribution of states and slower exchange dynamics in a lipid bilayer environment than in detergent micelles

(A and B) Comparison of the ^{19}F NMR spectra of apo (A) or agonist-bound (B) $A_{2A}R$ reconstituted in either lauryl maltose-neopentyl glycol (LMNG) micelles or phospholipid nanodiscs. Data for the detergent spectra were obtained from Ye et al. (2016) with permission from the authors.

to both ligand and G protein. As discussed below, spectral deconvolutions suggest the precoupled state is dynamic in the absence of G protein, which may be part of a mechanism for G protein recognition.

The redistribution of states upon formation of the complex with G protein is accompanied by changes in local dynamics. Spectral deconvolutions (Figures S4 and S5) reveal that A_3 is represented by a broad resonance in the absence of G protein, consistent with intermediate timescale sampling of a broad range of conformational sub-states (within the A_3 state). Addition of the G protein effectively limits exchange dynamics, resulting in a sharper, well-defined A_3 resonance. The narrower line width indicates restricted sampling of sub-states and an overall convergence into more stable configurations. This precoupled population likely does not contribute significantly to nucleotide exchange given its higher occurrence in the apo spectra. It is conceivable, however, that complexes adopting stable intermediate states are more allosterically enabled to transition into active conformers capable of GDP release leading to either basal or ligand-induced G protein activation.

A comparison of the activation series for partial- and full-agonist-bound $A_{2A}R$ suggests that A_1 and A_2 are two unique active states associated with G protein activation. While full agonist preferentially stabilizes A_1 (Figure 3D), the addition of either GDP-bound $G\alpha\beta\gamma$ or partial agonist enhances the A_2 fraction (Figures 3A–3D). Importantly, removal of GDP by apyrase further enhances the respective populations associated with A_1 and A_2, suggesting that these two states specifically facilitate nucleotide exchange and are favored by either a full agonist (A_1) or a partial agonist (A_2). The addition of an engineered mini-G protein (mini-G_s), previously designed to bind and stabilize the active state in the presence of agonist and without the use of the full heterotrimer (Carpenter and Tate, 2016), also stabilized A_1, albeit with little dependence on nucleotide (Figure S6). Together, the results suggest that $A_{2A}R$ can adopt a unique precoupled/intermediate state (A_3) that enables binding to the GDP-bound heterotrimer, in addition to distinct active-state conformers (A_1 and A_2) that facilitate GDP release through stabilization of a nucleotide-free G protein.

The above-mentioned interpretation provides a basis for understanding the ceiling effect in partial agonism. In the presence of heterotrimer, the precoupled fraction is in fact larger for the apo receptor than that observed with either partial or full agonist. However, the full-agonist-bound spectrum is distinguished by the A_1 state, while the partial-agonist-bound spectrum is distinguished by the A_2 state with an apparent A_1 fraction that is comparable to that of the apo receptor. The results imply that both A_1 and A_2 are signaling competent, while the A_1 conformer more efficiently enables GDP release and activation. Thus, a partial agonist will fail to promote maximal biological response at saturating concentrations of ligand, as the nucleotide exchange step is primarily driven by a less efficacious receptor state (A_2). The observation addresses a long-standing phenomenon in pharmacology, namely partial agonism, from a molecular ensemble perspective. Prior NMR studies in detergent micelles have identified that partial and full agonists establish unique activation intermediates using G protein mimetics (Frei et al., 2020; Solt et al., 2017; Ye et al., 2016). Using full heterotrimeric G proteins, we are now able to understand efficacy from the perspective of the effect of the ligand on the precoupling and nucleotide exchange steps. Note that upon removal of nucleotide through apyrase, the apo (+ G protein) spectrum also reveals a small increase in the A_1 fraction, which alongside A_2 would presumably be responsible for basal signaling (Figure 3A).

While A_1 and A_2 designate two different conformations that are distinguished by chemical shifts, the mechanism for their varied efficacy is likely complex and kinetically driven. A recent single-molecule fluorescence study of the β_2-adrenergic receptor showed that partial- and full-agonist-bound receptors facilitate

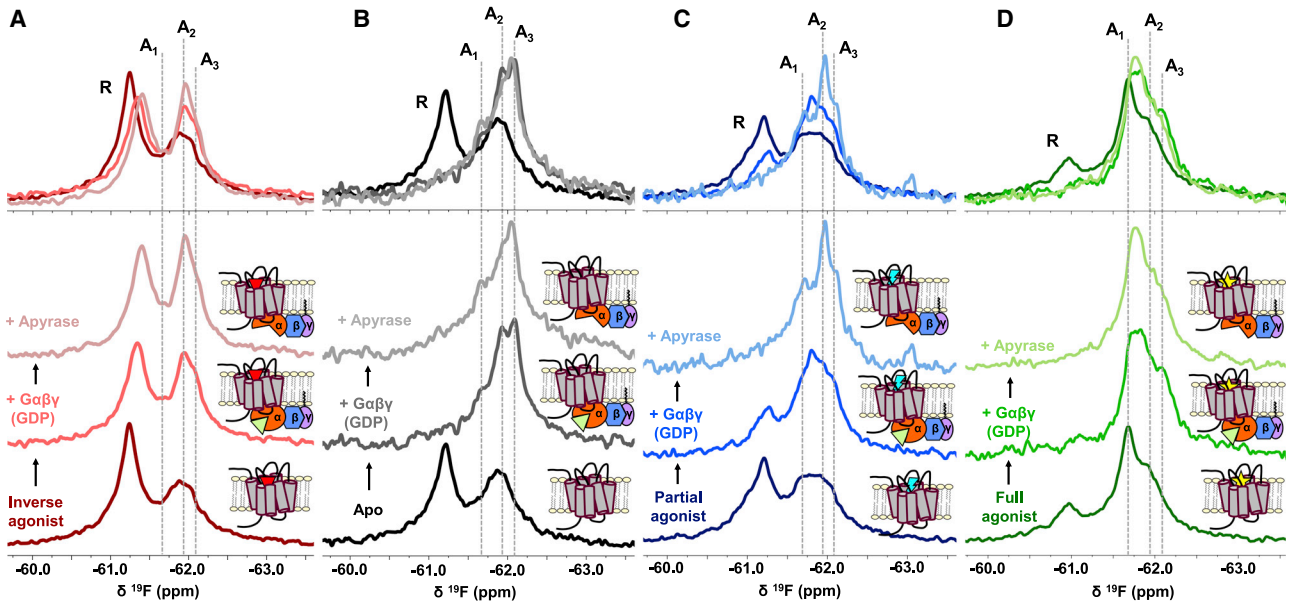

Figure 3. The precoupled state and nucleotide-free states are key facets of activation

(A–D) ^{19}F NMR spectra of A_{2A}R-V229C as a function of ligands, Gαβγ, and GDP. The addition of G_s heterotrimer (Gαβγ) and subsequently apyrase to inverse agonist-bound (A), apo (B), partial-agonist-bound (C), and full-agonist-bound (D) A_{2A}R enabled the assignment of at least three unique active state conformers as indicated by the gray dashed lines at −61.70 ppm (A_1), −61.95 ppm (A_2), and −62.10 ppm (A_3). Stabilization of representative states by the GDP-bound Gαβγ and nucleotide-free Gαβγ can be directly visualized in the overlaid spectra.

nucleotide exchange through different intermediates that affect rates of G protein binding and GDP release (Gregorio et al., 2017). The current NMR data demonstrate that the entire activation process is defined by a basis set of activation states (A_1–A_3) wherein equilibria and exchange kinetics are influenced by ligand, heterotrimer, and nucleotide. This builds upon recent advances in receptor NMR that used conformation-selective nanobodies (Frei et al., 2020; Solt et al., 2017; Staus et al., 2016), a valuable tool for stabilizing specific receptor states, but that does not capture the critical steps that define a GPCR's ability to facilitate nucleotide exchange. We note that while the current work suggests that the process is driven by conformational selection through three principle activation states, the true conformational landscape may be more complex and induced fit likely plays an important role especially at binding interfaces (Sušac et al., 2018).

Gβγ plays a key role in reinforcing allosteric pathways and signal transmission

The spectra in Figure 3 point to the importance of Gβγ as an allosteric chaperone in signal transduction. Compared with spectra in the presence of Gα alone (Figure 1), the intact heterotrimer significantly enhances the fraction of active conformers while allowing better delineation of the individual active states. To assess the relationship between states observed by NMR and the receptor's biological output, we conducted GTP hydrolysis assays using either G_sα or G_sαβγ in the presence of A_{2A}R bound to various ligands (Figure 4). As a guanine nucleotide exchange factor (GEF), A_{2A}R mediates nucleotide exchange and thereby accelerates GTP turnover. As expected, the presence of equimolar A_{2A}R resulted in an increase in cumulative GTP turnover by both G_sα and G_sαβγ over a 90-min period, in comparison with that of with G protein alone. Additionally, the effect of this enhancement is substantially higher for G_sαβγ than G_sα (Figure 4A), implying a greater level of receptor-mediated nucleotide exchange in the presence of Gβγ.

The magnitude of GEF activity, shown in Figure 4A, correlates expectedly with ligand efficacy (full agonist > partial agonist > apo > inverse agonist). Comparing these with respective ^{19}F NMR spectra challenges the classic two-state activation model (Figures S4). In general, the proportion of R* states (summation of the entire active ensemble) is not a predictor of efficacy. For example, while 92% of the apo-A_{2A}R-Gαβγ (nucleotide-free) spectrum is represented by R*, only 84% of the spectrum is represented by R* in the presence of the partial agonist. The discrepancy speaks to the weakness of a two-state (or three-state) model and underscores the importance of resolving the ensemble. Direct comparison of the ^{19}F NMR spectra and associated deconvolutions (Figures 3 and S7) show that efficacy in A_{2A}R is determined by the propensity of the receptor to populate states that are competent for nucleotide exchange (A_1 being more important than A_2). This mechanism will allow ligands with different molecular signatures and binding modes to reshape the receptor equilibrium and the distribution of A_1/A_2, resulting in a wide range of possible efficacy values.

Ligand dependence of GEF activity is only observed with the intact heterotrimer, as shown in Figure 4A. While the increase in GTP turnover correlates with ligand efficacy for G_sαβγ, the trend is absent for G_sα alone regardless of receptor concentration (Figure 4B). Hence, Gβγ appears to be important in translating ligand efficacy from the receptor orthosteric pocket to

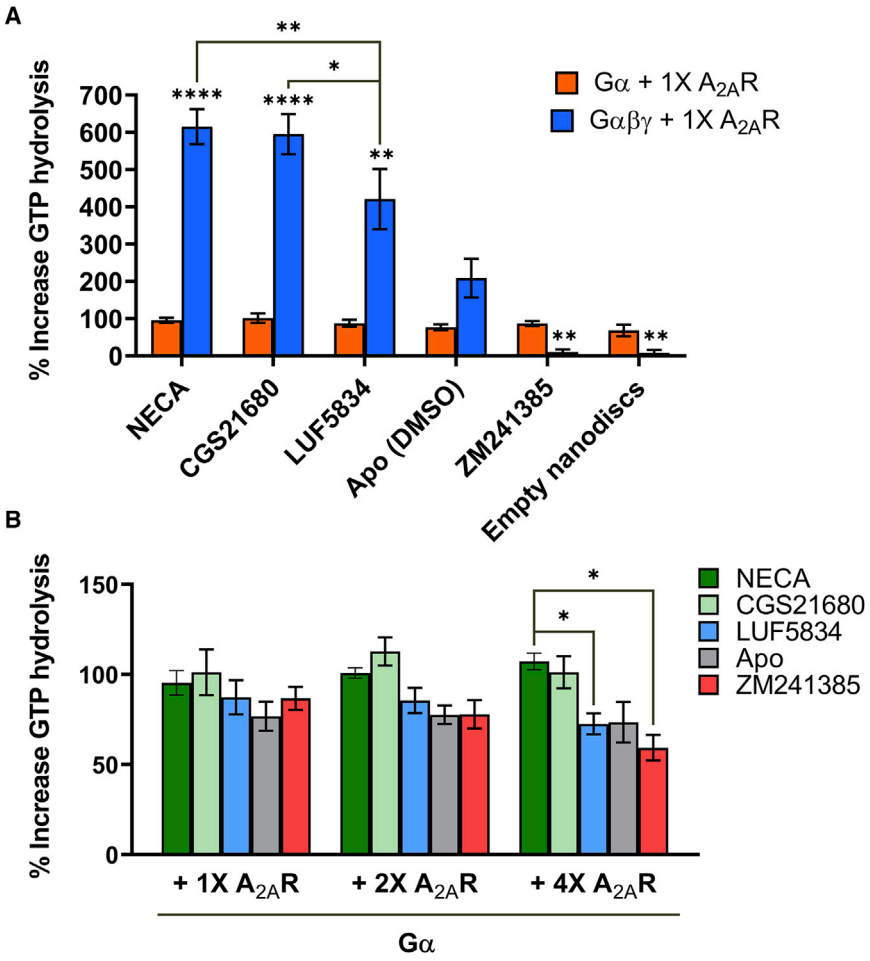

Figure 4. Gβγ enhances receptor-mediated nucleotide exchange and ligand dependence of GEF action

(A) Percent increase in GTP hydrolysis by either Gα or Gαβγ in the presence of one stoichiometric equivalence of $A_{2A}R$ bound to full agonists (NECA and CGS21680), partial agonist (LUF5834), inverse agonist (ZM241385), or no ligand, relative to the amount of GTP hydrolyzed by Gα or Gαβγ alone in the absence of $A_{2A}R$ over a 90-min period. Data represent mean ± SEM ($n \geq 3$). Asterisks directly above the bars represent statistical significance relative to the apo condition. Statistical significance was determined by two-way ANOVA followed by the Bonferroni (comparison of Gα and Gαβγ for each ligand) or the Tukey test (comparison of each ligand condition to each other). In the case of Gα, there is no significant difference between each ligand.

(B) Percent increase in GTP hydrolysis by Gα in the presence of one, two, or four stoichiometric equivalence of $A_{2A}R$ bound to full agonists (NECA and CGS21680), partial agonist (LUF5834), inverse agonist (ZM241385), or no ligand, relative to the amount of GTP hydrolyzed in the absence of $A_{2A}R$ over a 90-min period. Data represent mean ± SEM ($n \geq 3$). Statistical significance was determined by multiple t test using the Holm-Sidak method. *$p \leq 0.05$; **$p \leq 0.01$; ***$p \leq 0.001$; ****$p \leq 0.0001$.

the action of nucleotide exchange at Gα. While structures of GPCR-G protein complexes reveal weak (García-Nafría et al., 2018) to no direct contact between receptor and Gβγ, indirect interactions can be established via the Gα N-terminal helix that engages both ICL2 of the receptor and Gβ. A recent D_2 dopamine receptor-G_i structure in lipid bilayer revealed significant electrostatic interactions of Gβ with the charged phospholipid head group moieties, in addition to contacts with acyl moieties on Gγ (Yin et al., 2020). Gβγ can therefore be considered a conformational scaffold important for stabilizing the receptor-Gα interface, particularly in the context of the phospholipid bilayer (Oldham and Hamm, 2008; Smrcka and Fisher, 2019).

We evaluated the effects of Gβγ on ternary complex stability through native-polyacrylamide gel electrophoresis (native-PAGE). As expected, affinity between $A_{2A}R$ and G protein was strengthened in the presence of Gβγ (Figure 5A). GDP-bound G_sαβγ migrated as a single band with partial- and full-agonist-bound $A_{2A}R$, indicating the formation of tight complex in both cases. Note that due to negatively charged phospholipids, the bands for $A_{2A}R$-G_sαβγ complexes migrated further down the gel than G_sαβγ alone. The similar migration pattern observed between the full- and partial-agonist-bound ternary complex is consistent with surface plasmon resonance (SPR) data, which showed binding kinetics associated with receptor-G_sαβγ interactions to be similar between the two ligands (Figures 5B–5D). On the other hand, the migration patterns of G_sαβγ with apo receptor, as well as that of G_sα alone with receptor bound to either partial or full agonist, appear to be smeared, indicating weaker receptor-G protein interactions. Taken together, the data suggest that the difference in functional output provided by a partial-agonist-bound and a full-agonist-bound receptor is not due to differences in receptor affinity to G_sαβγ. Rather, efficacy is a consequence of the allosteric interplay between ligand, receptor, and the intact heterotrimer.

Building on prior computational studies that have identified allosteric pathways between the receptor and G protein (Fanelli et al., 2016; Lee et al., 2019), we focused specifically on how Gβγ facilitates signal transmission, using rigidity-transmission allostery (RTA) algorithms (Jacobs et al., 2001; Sljoka, 2021). This graph-theory-based analysis explores potential allosteric networks within the system. In this case, the system consists of a receptor-heterotrimer complex in the presence of agonist and GDP. Upon rigidification of the agonist NECA, a well-defined pathway emerges across the ternary complex (Figure 6A). Atoms within these regions are characterized by significant changes in their degrees of freedom—a sign of allosteric communication to the orthosteric binding site. This pathway passes through the Gα binding interface encompassing ICL2 of the receptor and the N- and C-terminal helices of Gα, via an allosteric network propagating across extracellular loops 1

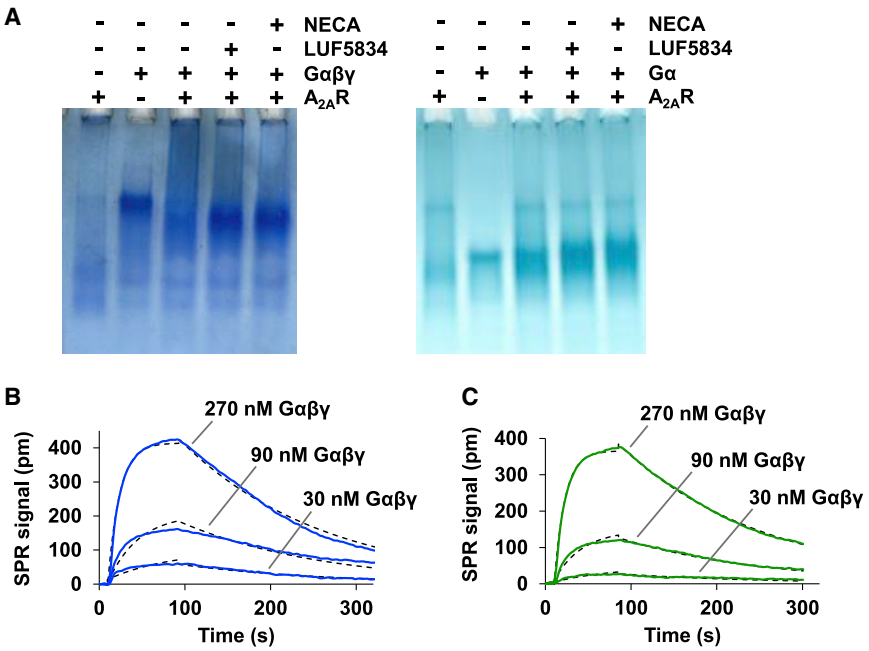

D

	k_{on} $(10^5\ M^{-1}s^{-1})$	k_{off} $(10^{-3}\ s^{-1})$	K_d (nM)
Partial agonist	2.4 ± 0.6	5 ± 2	19 ± 6
Full agonist	2.9 ± 0.6	5.3 ± 0.6	19 ± 3

Figure 5. The $A_{2A}R$-$G_s\alpha\beta\gamma$ interaction is characterized by similar affinity and binding kinetics when bound to a full agonist or a partial agonist

(A) $A_{2A}R$-G protein interactions assessed by native-PAGE. Note that due to negatively charged lipids and the natural size distribution of nanodiscs, $A_{2A}R$ migrated further down the gel and the corresponding band appears smeared relative to that in the presence of Gα and Gαβγ. Consequently, complexation with receptor resulted in a band for the $A_{2A}R$-Gαβγ complex that appeared lower on the gel than Gαβγ alone. This effect is absent in the case of Gα.

(B and C) Representative SPR binding curves (solid lines) for the interaction of Gαβγ with immobilized $A_{2A}R$ saturated with either partial agonist (B) or full agonist (C). Curves obtained at the three indicated concentrations were simultaneously fitted to a one-to-one binding model (dotted lines).

(D) SPR-derived K_d values and on/off rates for the interaction between $A_{2A}R$ and Gαβγ in the presence of indicated ligands. Data represent mean ± SD (n = 3).

and 2, TM2, TM3, TM7, regions of the Gα Ras domain, and regions of Gβ.

Remarkably, strong allosteric transmission is observed in three of the seven beta propellers and the helical region of Gβ that forms a coiled-coil interaction with the γ subunit (Figure 6A). These allosteric hotspots form multiple contacts with Gα, suggesting a means for Gβγ to contribute to signal transmission and serve as an allosteric chaperone. Given that ligand dependence of nucleotide exchange requires an intact heterotrimer, regulation of this process likely involves a concerted effort from both the receptor and the Gβγ subunit over the nucleotide-binding site. This would involve allosterically engaging conserved motifs and switch regions, many of which are part of this allosteric pathway (Figure 6B). Interestingly, phylogenetic analysis showed that Gα and Gβγ initially co-evolved as a signaling module apart from the GPCRs (Bradford et al., 2013). Therefore, it is likely that the receptor-specific regulatory role of Gβγ observed in our current data emerged later in organisms that adopted GPCR-dependent G protein signaling.

As the largest family of membrane proteins, GPCRs are the gateways to diverse cellular processes and are among the most important drug targets. While the accumulation of structures over the past two decades enabled efficient design of lead compounds, success of these drug discovery efforts has been limited. Subtype selectivity, efficacy, and signaling bias are major factors to be considered in designing drugs with low side effects, and it is increasingly recognized that understanding the dynamical aspects of receptor signaling is key to grasping these processes. While it is tempting to string together structural snapshots from crystallography and cryo-EM in formulating a mechanistic model for G protein coupling, NMR teaches us that activation is not a linear sequence of events. Rather, the functional states that we imagine to be necessary to equip the receptor for G protein coupling and subsequent activation are in fact sampled by the apo receptor. The equilibrium distribution of functional states, provided by ^{19}F NMR spectra in the presence of G protein with and without nucleotide, reflects the receptor's energy landscape at different steps along its activation pathway. Ligands and nucleotide not only remodel the landscape but also allosterically imbue the capacity for efficient exchange between functional states. A collection of such energy landscapes is illustrated in Figure 7 for $A_{2A}R$, where the receptor is envisaged to reversibly sample states along "reaction coordinates." Here, ^{19}F NMR reveals a conformational ensemble comprised of at least five key functional states—two inactive states (S_1 and S_2) differentiated by the switching of a conserved ionic lock and three active states associated with recognition and precoupling (A_3) and nucleotide exchange (A_1 and A_2). Ligands modulate both energies and lifetimes of these states, and multiple allosteric pathways are undoubtedly a common feature of GPCRs. In this study of $A_{2A}R$, A_1 is observed to be more efficacious and is preferentially stabilized by full agonist, while A_2 is preferentially stabilized by partial agonist. Although nucleotide exchange is achieved in the $G_s\alpha$ subunit, the entire heterotrimer plays a role in signal transmission where distinct allosteric pathways are suggested to traverse the nucleotide binding site via the $G_s\alpha$-$A_{2A}R$ and the $G_s\alpha$-Gβ interfaces.

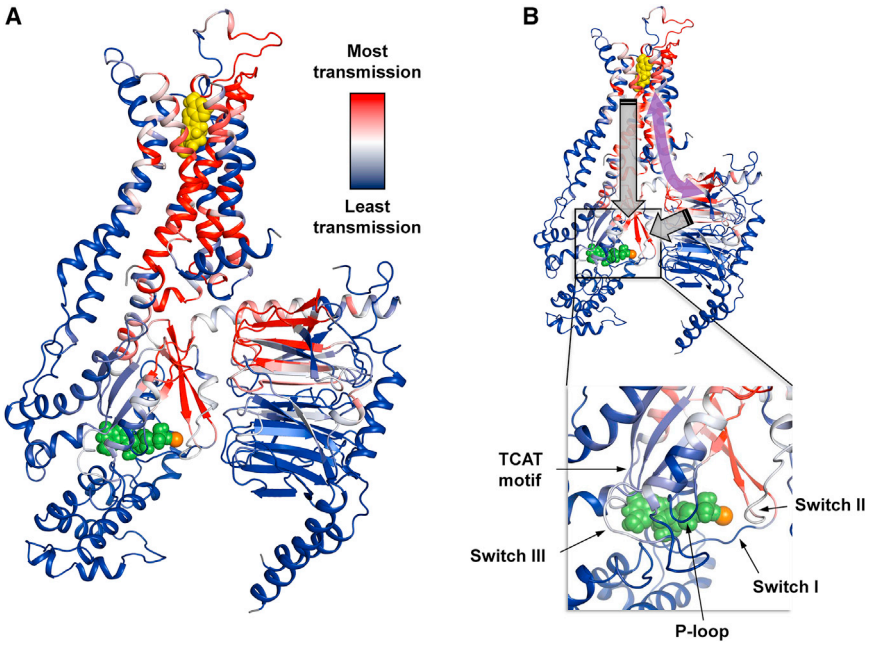

Figure 6. Gβγ plays a key role in reinforcing allosteric pathways and signal transmission

(A) The allosteric network within the ternary complex is revealed through rigidity theory analysis. Here, allosteric transmission is measured by regiospecific changes in degrees of freedom (red/blue color gradient bar) experienced upon rigidification of the agonist NECA (yellow spheres). An allosteric pathway can be defined between the orthosteric pocket and $G_s\alpha\beta\gamma$ that, in turn, connects with the nucleotide-binding region. Green spheres designate GDP, and the orange sphere represents Mg^{2+}.

(B) The symmetric property of allosteric transmission means that Gβγ, despite not being in direct contact with the receptor, may impart allosteric effects on remote regions in the pathway such as the orthosteric binding site (curved purple arrow). Nucleotide exchange involves structural rearrangement of Gα facilitated by movements of conserved motifs (annotated inset). This likely requires a concerted interplay between receptor and both the Gα and Gβγ subunits acting on the nucleotide-binding pocket (gray block arrows).

The energy landscape perspective provides the opportunity to advance our understanding of the mechanism of action for both orthosteric and allosteric drugs in $A_{2A}R$ and possibly other GPCRs. For example, the action of an inverse agonist can be precisely studied in terms of its capacity to alter the strength of the ionic lock and the inactive/active equilibrium. Similarly, the efficacy of both partial and full agonists in addition to allosteric modulators can be understood in terms of their capacity to stabilize individual activation intermediates. Future NMR relaxation studies may also add kinetic details and thus energy barrier representations to this description. Finally, we note that NMR initiatives such as those described above may help to identify the appropriate adjuvants necessary to stabilize given functional states of interest as a prelude to cryo-EM, X-ray crystallography, and the production of state-specific GPCR antibodies.

Limitations of study

The mechanistic interpretations presented in the current study are based on the observation of a single probe on TM6. While the V229C location is excellent for probing conformational changes of TM6, the study is limited in terms of addressing cooperativity between different domains of the receptor such as the extracellular and intracellular loops as well as other transmembrane helices. Additionally, while the methods used here are applicable to the study of receptors at large, our results are specific to $A_{2A}R$ and may not generalize to all GPCRs.

STAR★METHODS

Detailed methods are provided in the online version of this paper and include the following:

- KEY RESOURCES TABLE
- RESOURCE AVAILABILITY
  - Lead contact
  - Materials availability
  - Data and code availability
- EXPERIMENTAL MODEL AND SUBJECT DETAILS
  - Microbes
  - Cell lines
- METHOD DETAILS
  - $A_{2A}R$ expression, purification, and labeling
  - Nanodisc assembly and purification
  - $G_s\alpha$ expression and purification
  - Mini-$G_s\alpha$ expression and purification
  - Gβγ expression and purification
  - NMR experiments
  - NMR spectral deconvolution
  - NMR spectral assignments and validation of chemical shifts
  - GTP hydrolysis experiments
  - Native-PAGE
  - SPR experiments
  - $A_{2A}R$-Gαβγ modeling
  - Allostery computations using rigidity transmission theory
- QUANTIFICATION AND STATISTICAL ANALYSIS

ACKNOWLEDGMENTS

This work was supported by the Canadian Institutes of Health Research (CIHR) Operating Grant MOP-43998 to R.S.P., the National Institute of General Medical Sciences grants GM106990 and GM083118 to R.K.S., and the MEXT/JSPS KAKENHI no. JP19K23721 to D.P.T. and no. JP19H03191 to A.K. S.K.H. is supported by Alexander Graham Bell Canada Graduate Scholarship-Doctoral from NSERC. A.S. was supported by CREST, Japan Science and Technology Agency (JST), Japan, JPMJCR1402. We thank Dr. Oliver Ernst and Dr. Ned Van Eps for helpful discussions and for providing plasmids with the $G_s\alpha$ and the mini-$G_s\alpha$ sequence. Special thanks to Dr. Marko Jovic from Nicoya Lifesciences for help

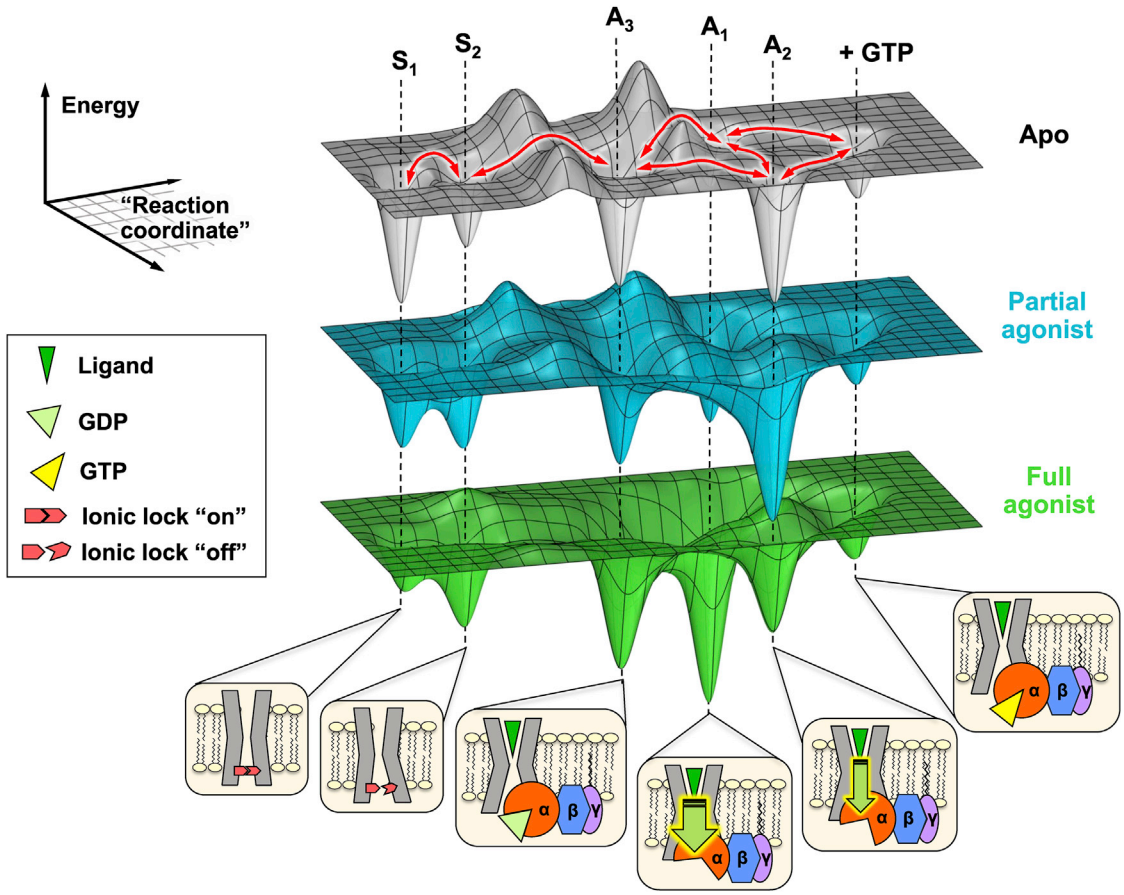

Figure 7. $A_{2A}R$ populates a dynamic energy landscape encompassing key functional states associated with activation, G protein coupling, and nucleotide exchange

The conformational ensemble of $A_{2A}R$ is represented by five key functional states—two inactive states (S_1 and S_2) differentiated by the switching of a conserved ionic lock and three active states (A_1, A_2, and A_3) associated with G protein coupling. A_3, an intermediate or precoupled state, plays a role in the recognition and binding of the G protein. A_1 and A_2, on the other hand, are responsible for GDP release and stabilization of the nucleotide-free complex. While A_1 is more efficacious (thicker downward arrow) and stabilized to a larger extent by the full agonist, A_2 is less efficacious (thinner downward arrow) and is preferentially stabilized by a partial agonist. Although not included in this work, we also envision a state where the receptor forms a transiently stable complex with a GTP-bound G protein. The activation pathway can be considered as a series of reversible transformations between states (red arrows), whose populations and lifetimes are modulated through the presence of ligands, G protein, nucleotides, and other allosteric factors.

with SPR data analysis, Dr. Voula Kanelis for access to her lab equipment, Dmitry Pichugin for NMR spectrometer maintenance, and Zixin Chen for artistic input. In memory of our cherished colleague and friend, Prof. Éric Marsault, at the University of Sherbrooke.

AUTHOR CONTRIBUTIONS

S.K.H. and R.S.P. designed the research. S.K.H. performed protein expression and purification for $A_{2A}R$ and $G_s\alpha$. S.K.H. performed the NMR experiments, GTP hydrolysis experiments, native-PAGE, SPR experiments, and all associated data analysis. A.P., N.L.V., and S.K.H. conducted expression and purification of $G\beta\gamma$. D.P.T. and A.K. performed computational modeling of the $A_{2A}R$-$G_s\alpha$ complex. A.S. performed the RTA analysis. S.K.H. and R.S.P. prepared the manuscript. A.S. supervised the computational studies. R.K.S. provided assistance with $G\beta\gamma$ and the manuscript. R.S.P. supervised the project.

DECLARATION OF INTERESTS

The authors declare no competing interests.

Received: August 31, 2020
Revised: December 2, 2020
Accepted: February 17, 2021
Published: March 19, 2021

REFERENCES

Ballesteros, J.A., and Weinstein, H. (1995). Integrated methods for the construction of three-dimensional models and computational probing of structure-function relations in G protein-coupled receptors. Methods Neurosci. *25*, 366–428.

Ballesteros, J.A., Jensen, A.D., Liapakis, G., Rasmussen, S.G.F., Shi, L., Gether, U., and Javitch, J.A. (2001). Activation of the β 2-adrenergic receptor involves disruption of an ionic lock between the cytoplasmic ends of transmembrane segments 3 and 6. J. Biol. Chem. *276*, 29171–29177.

Bockenhauer, S., Fürstenberg, A., Yao, X.J., Kobilka, B.K., and Moerner, W.E. (2011). Conformational dynamics of single G protein-coupled receptors in solution. J. Phys. Chem. B *115*, 13328–13338.

Bradford, W., Buckholz, A., Morton, J., Price, C., Jones, A.M., and Urano, D. (2013). Eukaryotic G protein signaling evolved to require G protein-coupled receptors for activation. Sci. Signal. *6*, ra37.

Braun, S., and Levitzki, A. (1979). Adenosine receptor permanently coupled to turkey erythrocyte adenylate cyclase. Biochemistry *18*, 2134–2138.

Carpenter, B., and Tate, C.G. (2016). Engineering a minimal G protein to facilitate crystallisation of G protein-coupled receptors in their active conformation. Protein Eng. Des. Sel. *29*, 583–594.

Carpenter, B., Nehmé, R., Warne, T., Leslie, A.G.W., and Tate, C.G. (2016). Erratum: Structure of the adenosine A_{2A} receptor bound to an engineered G protein. Nature *538*, 542.

Casiraghi, M., Damian, M., Lescop, E., Point, E., Moncoq, K., Morellet, N., Levy, D., Marie, J., Guittet, E., Banères, J.L., and Catoire, L.J. (2016). Functional modulation of a G protein-coupled receptor conformational landscape in a lipid bilayer. J. Am. Chem. Soc. *138*, 11170–11175.

Cavanagh, J., Skelton, N.J., Fairbrother, W.J., Rance, M., and Palmer, A.G., III. (2007). Protein NMR Spectroscopy (Academic Press).

Clark, L.D., Dikiy, I., Chapman, K., Rödström, K.E.J., Aramini, J., LeVine, M.V., Khelashvili, G., Rasmussen, S.G.F., Gardner, K.H., and Rosenbaum, D.M. (2017). Ligand modulation of sidechain dynamics in a wild-type human GPCR. eLife *6*, 1–27.

Congreve, M., de Graaf, C., Swain, N.A., and Tate, C.G. (2020). Impact of GPCR Structures on Drug Discovery. Cell *181*, 81–91.

Daura, X., Gademann, K., Jaun, B., Seebach, D., van Gunsteren, W.F., and Mark, A.E. (1999). Peptide Folding: When Simulation Meets Experiment. Angew. Chemie Int. *38*, 236–240.

de Lera Ruiz, M., Lim, Y.H., and Zheng, J. (2014). Adenosine A2A receptor as a drug discovery target. J. Med. Chem. *57*, 3623–3650.

Doré, A.S., Robertson, N., Errey, J.C., Ng, I., Hollenstein, K., Tehan, B., Hurrell, E., Bennett, K., Congreve, M., Magnani, F., et al. (2011). Structure of the adenosine A(2A) receptor in complex with ZM241385 and the xanthines XAC and caffeine. Structure *19*, 1283–1293.

Dror, R.O., Arlow, D.H., Maragakis, P., Mildorf, T.J., Pan, A.C., Xu, H., Borhani, D.W., and Shaw, D.E. (2011). Activation mechanism of the β2-adrenergic receptor. Proc. Natl. Acad. Sci. USA *108*, 18684–18689.

Du, Y., Duc, N.M., Rasmussen, S.G.F., Hilger, D., Kubiak, X., Wang, L., Bohon, J., Kim, H.R., Wegrecki, M., Asuru, A., et al. (2019). Assembly of a GPCR-G protein complex. Cell *177*, 1232–1242.e11.

Eddy, M.T., Lee, M.Y., Gao, Z.G., White, K.L., Didenko, T., Horst, R., Audet, M., Stanczak, P., McClary, K.M., Han, G.W., et al. (2018). Allosteric coupling of drug binding and intracellular signaling in the A2A adenosine receptor. Cell *172*, 68–80.e12.

Effendi, W.I., Nagano, T., Kobayashi, K., and Nishimura, Y. (2020). Focusing on Adenosine Receptors as a Potential Targeted Therapy in Human Diseases. Cells *9*, 785.

Fanelli, F., Felline, A., Raimondi, F., and Seeber, M. (2016). Structure network analysis to gain insights into GPCR function. Biochem. Soc. Trans. *44*, 613–618.

Fredriksson, R., Lagerström, M.C., Lundin, L.G., and Schiöth, H.B. (2003). The G-protein-coupled receptors in the human genome form five main families. Phylogenetic analysis, paralogon groups, and fingerprints. Mol. Pharmacol. *63*, 1256–1272.

Frei, J.N., Broadhurst, R.W., Bostock, M.J., Solt, A., Jones, A.J.Y., Gabriel, F., Tandale, A., Shrestha, B., and Nietlispach, D. (2020). Conformational plasticity of ligand-bound and ternary GPCR complexes studied by 19F NMR of the β1-adrenergic receptor. Nat. Commun. *11*, 1–14.

Galés, C., Van Durm, J.J.J., Schaak, S., Pontier, S., Percherancier, Y., Audet, M., Paris, H., and Bouvier, M. (2006). Probing the activation-promoted structural rearrangements in preassembled receptor-G protein complexes. Nat. Struct. Mol. Biol. *13*, 778–786.

García-Nafría, J., Lee, Y., Bai, X., Carpenter, B., and Tate, C.G. (2018). Cryo-EM structure of the adenosine A_{2A} receptor coupled to an engineered heterotrimeric G protein. eLife *7*, 1–19.

Gregorio, G.G., Masureel, M., Hilger, D., Terry, D.S., Juette, M., Zhao, H., Zhou, Z., Perez-Aguilar, J.M., Hauge, M., Mathiasen, S., et al. (2017). Single-molecule analysis of ligand efficacy in β_2AR-G-protein activation. Nature *547*, 68–73.

Guerrero, A. (2018). A2A Adenosine Receptor Agonists and their Potential Therapeutic Applications. An Update. Curr. Med. Chem. *25*, 3597–3612.

Hagn, F., Etzkorn, M., Raschle, T., and Wagner, G. (2013). Optimized phospholipid bilayer nanodiscs facilitate high-resolution structure determination of membrane proteins. J. Am. Chem. Soc. *135*, 1919–1925.

Hauser, A.S., Attwood, M.M., Rask-Andersen, M., Schiöth, H.B., and Gloriam, D.E. (2017). Trends in GPCR drug discovery: new agents, targets and indications. Nat. Rev. Drug Discov. *16*, 829–842.

Hoover, W.G. (1985). Canonical dynamics: Equilibrium phase-space distributions. Phys. Rev. A Gen. Phys. *31*, 1695–1697.

Isogai, S., Deupi, X., Opitz, C., Heydenreich, F.M., Tsai, C.J., Brueckner, F., Schertler, G.F.X., Veprintsev, D.B., and Grzesiek, S. (2016). Backbone NMR reveals allosteric signal transduction networks in the β1-adrenergic receptor. Nature *530*, 237–241.

Jacobs, D.J., Rader, A.J., Kuhn, L.A., and Thorpe, M.F. (2001). Protein flexibility predictions using graph theory. Proteins *44*, 150–165.

Jorgensen, W.L., Chandrasekhar, J., Madura, J.D., Impey, R.W., and Klein, M.L. (1983). Comparison of simple potential functions for simulating liquid water. J. Chem. Phys. *79*, 926–935.

Kaya, A.I., Lokits, A.D., Gilbert, J.A., Iverson, T.M., Meiler, J., and Hamm, H.E. (2014). A conserved phenylalanine as a relay between the α5 helix and the GDP binding region of heterotrimeric Gi protein α subunit. J. Biol. Chem. *289*, 24475–24487.

Kofuku, Y., Ueda, T., Okude, J., Shiraishi, Y., Kondo, K., Mizumura, T., Suzuki, S., and Shimada, I. (2014). Functional dynamics of deuterated β2 -adrenergic receptor in lipid bilayers revealed by NMR spectroscopy. Angew. Chem. Int. Ed. Engl. *53*, 13376–13379.

Lee, S., Nivedha, A.K., Tate, C.G., and Vaidehi, N. (2019). Dynamic role of the G protein in stabilizing the active state of the adenosine A2A receptor. Structure *27*, 703–712.e3.

Liu, W., Chun, E., Thompson, A.A., Chubukov, P., Xu, F., Katritch, V., Han, G.W., Roth, C.B., Heitman, L.H., IJzerman, A.P., et al. (2012). Structural basis for allosteric regulation of GPCRs by sodium ions. Science *337*, 232–236.

Liu, X., Xu, X., Hilger, D., Aschauer, P., Tiemann, J.K.S., Du, Y., Liu, H., Hirata, K., Sun, X., Guixà-González, R., et al. (2019). Structural Insights into the Process of GPCR-G Protein Complex Formation. Cell *177*, 1243–1251.e12.

Maier, J.A., Martinez, C., Kasavajhala, K., Wickstrom, L., Hauser, K.E., and Simmerling, C. (2015). ff14SB: Improving the Accuracy of Protein Side Chain and Backbone Parameters from ff99SB. J. Chem. Theory Comput. *11*, 3696–3713.

Manglik, A., Kim, T.H., Masureel, M., Altenbach, C., Yang, Z., Hilger, D., Lerch, M.T., Kobilka, T.S., Thian, F.S., Hubbell, W.L., et al. (2015). Structural insights into the dynamic process of β2 -adrenergic receptor signaling. Cell *161*, 1101–1111.

Medkova, M., Preininger, A.M., Yu, N.J., Hubbell, W.L., and Hamm, H.E. (2002). Conformational changes in the amino-terminal helix of the G protein α(i1) following dissociation from Gbetagamma subunit and activation. Biochemistry *41*, 9962–9972.

Mondal, S., Hsiao, K., and Goueli, S.A. (2015). A homogenous bioluminescent system for measuring GTPase, GTPase activating protein, and guanine nucleotide exchange factor activities. Assay Drug Dev. Technol. *13*, 444–455.

Nanoff, C., and Stiles, G.L. (1993). Solubilization and characterization of the A2-adenosine receptor. J. Recept. Res. *13*, 961–973.

Neubig, R.R. (1994). Membrane organization in G-protein mechanisms. FASEB J. *8*, 939–946.

Nobles, M., Benians, A., and Tinker, A. (2005). Heterotrimeric G proteins precouple with G protein-coupled receptors in living cells. Proc. Natl. Acad. Sci. USA *102*, 18706–18711.

Nosé, S. (1984). A unified formulation of the constant temperature molecular dynamics methods. J. Chem. Phys. *81*, 511–519.

Nygaard, R., Zou, Y., Dror, R.O., Mildorf, T.J., Arlow, D.H., Manglik, A., Pan, A.C., Liu, C.W., Fung, J.J., Bokoch, M.P., et al. (2013). The dynamic process of β(2)-adrenergic receptor activation. Cell *152*, 532–542.

Oldham, W.M., and Hamm, H.E. (2008). Heterotrimeric G protein activation by G-protein-coupled receptors. Nat. Rev. Mol. Cell Biol. *9*, 60–71.

Park, P.S.-H., Lodowski, D.T., and Palczewski, K. (2008). Activation of G protein-coupled receptors: beyond two-state models and tertiary conformational changes. Annu. Rev. Pharmacol. Toxicol. *48*, 107–141.

Parrinello, M., and Rahman, A. (1981). Polymorphic transitions in single crystals: A new molecular dynamics method. J. Appl. Physiol. *52*, 7182–7190.

Provasi, D., Artacho, M.C., Negri, A., Mobarec, J.C., and Filizola, M. (2011). Ligand-induced modulation of the free-energy landscape of G protein-coupled receptors explored by adaptive biasing techniques. PLoS Comput. Biol. *7*, e1002193.

Rebois, R.V., and Hébert, T.E. (2003). Protein complexes involved in heptahelical receptor-mediated signal transduction. Receptors Channels *9*, 169–194.

Sljoka, A. (2021). Probing Allosteric Mechanism with Long-Range Rigidity Transmission Across Protein Networks. Methods Mol. Biol. *2253*, 61–75.

Smrcka, A.V., and Fisher, I. (2019). G-protein βγ subunits as multi-functional scaffolds and transducers in G-protein-coupled receptor signaling. Cell. Mol. Life Sci. *76*, 4447–4459.

Solt, A.S., Bostock, M.J., Shrestha, B., Kumar, P., Warne, T., Tate, C.G., and Nietlispach, D. (2017). Insight into partial agonism by observing multiple equilibria for ligand-bound and G_s-mimetic nanobody-bound β_1-adrenergic receptor. Nat. Commun. *8*, 1795.

Sounier, R., Mas, C., Steyaert, J., Laeremans, T., Manglik, A., Huang, W., Kobilka, B.K., Déméné, H., and Granier, S. (2015). Propagation of conformational changes during μ-opioid receptor activation. Nature *524*, 375–378.

Staus, D.P., Strachan, R.T., Manglik, A., Pani, B., Kahsai, A.W., Kim, T.H., Wingler, L.M., Ahn, S., Chatterjee, A., Masoudi, A., et al. (2016). Allosteric nanobodies reveal the dynamic range and diverse mechanisms of G-protein-coupled receptor activation. Nature *535*, 448–452.

Sušac, L., Eddy, M.T., Didenko, T., Stevens, R.C., and Wüthrich, K. (2018). A_{2A} adenosine receptor functional states characterized by ^{19}F-NMR. Proc. Natl. Acad. Sci. USA *115*, 12733–12738.

Van Eps, N., Caro, L.N., Morizumi, T., Kusnetzow, A.K., Szczepek, M., Hofmann, K.P., Bayburt, T.H., Sligar, S.G., Ernst, O.P., and Hubbell, W.L. (2017). Conformational equilibria of light-activated rhodopsin in nanodiscs. Proc. Natl. Acad. Sci. USA *114*, E3268–E3275.

Vogel, R., Mahalingam, M., Lüdeke, S., Huber, T., Siebert, F., and Sakmar, T.P. (2008). Functional role of the "ionic lock"–an interhelical hydrogen-bond network in family A heptahelical receptors. J. Mol. Biol. *380*, 648–655.

Wang, J., Wolf, R.M., Caldwell, J.W., Kollman, P.A., and Case, D.A. (2004). Development and testing of a general amber force field. J. Comput. Chem. *25*, 1157–1174.

Weis, W.I., and Kobilka, B.K. (2018). The molecular basis of G protein–coupled receptor activation. Annu. Rev. Biochem. *87*, 897–919.

Weiss, H.M., and Grisshammer, R. (2002). Purification and characterization of the human adenosine A(2a) receptor functionally expressed in Escherichia coli. Eur. J. Biochem. *269*, 82–92.

Weiss, J.M., Morgan, P.H., Lutz, M.W., and Kenakin, T.P. (1996). The cubic ternary complex receptor-occupancy model I. Model description. J. Theor. Biol. *178*, 151–167.

Whiteley, W. (2005). Counting out to the flexibility of molecules. Phys. Biol. *2*, S116–S126.

Wu, F., Williams, L.M., Abdul-ridha, A., Gunatilaka, A., Vaid, T.M., Kocan, M., Whitehead, A.R., Griffin, M.D.W., Bathgate, R.A.D., Scott, D.J., et al. (2020). Probing the correlation between ligand efficacy and conformational diversity at the α1A-adrenoreceptor reveals allosteric coupling of its microswitches. J. Biol. Chem. *295*, 7404–7417.

Ye, L., Larda, S.T., Frank Li, Y.F., Manglik, A., and Prosser, R.S. (2015). A comparison of chemical shift sensitivity of trifluoromethyl tags: optimizing resolution in ^{19}F NMR studies of proteins. J. Biomol. NMR *62*, 97–103.

Ye, L., Van Eps, N., Zimmer, M., Ernst, O.P., and Prosser, R.S. (2016). Activation of the A2A adenosine G-protein-coupled receptor by conformational selection. Nature *533*, 265–268.

Ye, L., Neale, C., Sljoka, A., Lyda, B., Pichugin, D., Tsuchimura, N., Larda, S.T., Pomès, R., García, A.E., Ernst, O.P., et al. (2018). Mechanistic insights into allosteric regulation of the A_{2A} adenosine G protein-coupled receptor by physiological cations. Nat. Commun. *9*, 1372.

Yin, J., Chen, K.M., Clark, M.J., Hijazi, M., Kumari, P., Bai, X.C., Sunahara, R.K., Barth, P., and Rosenbaum, D.M. (2020). Structure of a D2 dopamine receptor-G-protein complex in a lipid membrane. Nature *584*, 125–129.

Yu, F., Zhu, C., Xie, Q., and Wang, Y. (2020). Adenosine A_{2A} Receptor Antagonists for Cancer Immunotherapy. J. Med. Chem. *63*, 12196–12212.

Zheng, J., Zhang, X., and Zhen, X. (2019). Development of Adenosine A_{2A} Receptor Antagonists for the Treatment of Parkinson's Disease: A Recent Update and Challenge. ACS Chem. Neurosci. *10*, 783–791.

STAR★METHODS

KEY RESOURCES TABLE

REAGENT or RESOURCE	SOURCE	IDENTIFIER
Bacterial and virus strains		
Escherichia coli BL21 (DE3)	Invitrogen	Cat#: C600003
Autographa californica nuclear polyhedrosis virus	ATCC	ATCC: VR-1344
Chemicals, peptides, and recombinant proteins		
2-bromo-N-(4-(trifluoromethyl)phenyl) acetamide (BTFMA)	Apollo Scientific	Cat#: PC8478
CGS21680	Tocris	Cat#: 1063
5′-N-Ethylcarboxamidoadenosine (NECA)	Tocris	Cat#: 1691
LUF 5834	Tocris	Cat#: 4603
ZM 241385	Tocris	Cat#: 1036
Xanthine amine congener (XAC)	Santa Cruz Biotechnology	Cat#: sc-255717A
Guanosine 5′-diphosphate (GDP)	Sigma-Aldrich	Cat#: 51060
Apyrase from potato (recombinant, expressed in *P. pastoris*)	Sigma-Aldrich	Cat#: A6237
n-Dodecyl-β-D-Maltoside (DDM)	Anatrace	Cat#: D310
Lauryl Maltose Neopentyl Glycol (LMNG)	Anatrace	Cat#: NG310
Cholesteryl hemisuccinate (CHS)	Sigma-Aldrich	Cat#: C6512
1-palmitoyl-2-oleoyl-glycero-3-phosphocholine (POPC)	Avanti Polar Lipids	Cat#: 850457C
1-palmitoyl-2-oleoyl-sn-glycero-3-phospho-(1'-rac-glycerol) (POPG)	Avanti Polar Lipids	Cat#: 840457C
Bio-Beads SM-2 Resin	Bio-Rad	Cat#: 1523920
HiLoad 16/600 Superdex 200 pg size exclusion column	Cytiva	Cat#: GE28-9893-35
TALON Metal Affinity Resin	Takara	Cat#: 635503
Affi-Gel 10	Bio-Rad	Cat#: 1536099
Macro-Prep High Q Resin	Bio-Rad	Cat#: 1560040
SPR NTA sensor chip	Nicoya	Cat#: SEN-AU-100-10-NTA
4–15% Mini-PROTEAN TGX Precast Protein Gels	Bio-Rad	Cat#: 4561086
Critical commercial assays		
GTPase-Glo	Promega	Cat#: V7681
Deposited data		
$A_{2A}R$ bound to NECA and mini-$G_s\alpha$	Carpenter et al., 2016	PDB: 5G53
GDP-bound G_s heterotrimer	Liu et al., 2019	PDB: 6EG8
Experimental models: cell lines		
Spodoptera frugiperda: Sf9 cells	ATCC	ATCC: CRL-1711
Pichia pastoris: strain SMD 1163	Invitrogen	N/A
Recombinant DNA		
Plasmid: pET15b containing $G_s\alpha$	Oliver Ernst lab, University of Toronto	N/A
Plasmid: pET15b containing Mini-$G_s\alpha$	Oliver Ernst lab, University of Toronto	N/A
Plasmid: pPIC9K_Fα-Factor–Flag–TEV-A2aARTr316-H10_V229C	Ye et al., 2016	N/A

(*Continued on next page*)

Continued

REAGENT or RESOURCE	SOURCE	IDENTIFIER
Software and algorithms		
MestReNova version 12.0.4 or higher	Mestrelab Research	https://mestrelab.com/
TraceDrawer 1.6.1	Ridgeview Instruments	https://www.ligandtracer.com/product/tracedrawer/
MODELER 9.21	Sali lab, University of California San Francisco	https://salilab.org/modeller/9.21/release.html
FIRST 5.2	Jacobs et al., 2001	https://github.com/psa-lab/proflex
MATLAB R2020a	MathWorks	https://www.mathworks.com/products/matlab.html

RESOURCE AVAILABILITY

Lead contact

Further information and requests for resources and reagents should be directed to and will be fulfilled by the lead contact, Scott Prosser (scott.prosser@utoronto.ca).

Materials availability

This study did not generate new unique reagents.

Data and code availability

The raw data, code, and algorithms used in this study are available from the corresponding authors upon request.

EXPERIMENTAL MODEL AND SUBJECT DETAILS

Microbes

Pichia pastoris SMD 1163 (*Δhis4 Δpep4 Δprb1*) cells were cultured in YPD, BMGY, and BMMY media. *Escherichia coli* BL21 (DE3) cells were cultured in LB medium.

Cell lines

Spodoptera frugiperda Sf9 cells were cultured in I-Max insect cell culture medium. The cell lines used in this study have not been authenticated.

METHOD DETAILS

$A_{2A}R$ expression, purification, and labeling

Plasmid construction, transformation, and colony screening has been described previously (Ye et al., 2016). Briefly, the plasmid pPIC9K_Fα-Factor–Flag–TEV-A2aARTr316-H10_V229C containing the human $A_{2A}R$ gene with a truncated C-terminal tail and the V229C mutation was transformed into *Pichia pastoris* (*P. pastoris*) SMD 1163 (*Δhis4 Δpep4 Δprb1*). A single colony of *P. pastoris* containing high copy number of the gene encoding $A_{2A}R$-V229C was inoculated into 200 mL of YPD medium (1% (w/v) yeast extract, 2% (w/v) peptone, 2% (w/v) glucose, and 0.2 mg/mL G418) and grown at 30°C for 24-36 h. This starter culture was inoculated into 2 L of BMGY medium (1% (w/v) yeast extract, 2% (w/v) peptone, 1.34% (w/v) yeast nitrogenase base (YNB) without amino acids, 100 mM sodium phosphate (pH 6.5), 0.4 mg/L biotin, 1% (v/v) glycerol, and 100 μg/mL ampicillin), grown at 30°C for 24 h, then transferred to a bioreactor (Genesis, Solaris Biotechnology) containing 12 L of BMMY medium without methanol (1% (w/v) yeast extract, 2% (w/v) peptone, 1.34% (w/v) YNB without amino acids, 0.4 mg/L biotin, 0.4 g/L histidine, 2% (v/v) DMSO, 5 mM theophylline, 100 μg/mL ampicillin, and 0.1 mL/L antifoam A. pH was maintained at 6.5 and dissolved oxygen was maintained at 30%). The culture was grown for 3 h at 19°C, then induced with 0.5% (v/v) methanol every 12 h for a total of 72 h. Cells were harvested by centrifugation at 4,000 g for 30 min, flash-frozen with liquid N_2, and stored at −80°C.

Cell pellets were resuspended in ice-cold lysis buffer (50 mM HEPES, pH 7.4, 300 mM NaCl, 4 mM theophylline, 5 mM 6-aminocaproic acid, 5 mM benzamidine, and 10% glycerol) and lysed using a microfluidizer (LM 20, ATS Scientific) at 20,000 psi in 2 passes. The lysate was centrifuged at 8,000 g for 30 min. The supernatant was collected and centrifuged at 100,000 g for 90 min, and the resulting pellet was resuspended in membrane solubilization buffer (50 mM HEPES, pH 7.4, 300 mM NaCl, 4 mM theophylline, 1 mM 6-aminocaproic acid, 1 mM benzamidine, 0.75% lauryl maltose neopentyl glycol (LMNG), and 0.05% cholesteryl hemisuccinate (CHS)) at 4°C overnight with gentle stirring. The solubilized membrane was centrifuged at 10,000 g for 1 h. Supernatant was collected and incubated with TALON resin (Takara) at 4°C for 12-24 h with gentle mixing.

The A_{2A}R-bound TALON resin was washed with 5 bed-volumes of labeling buffer (50 mM HEPES, pH 7.4, 300 mM NaCl, 0.05% LMNG, and 0.005% CHS), then incubated with 2 bed-volumes of degassed labeling buffer containing 200 μM 2-bromo-N-(4-(trifluoromethyl)phenyl)acetamide (BTFMA) at 4°C overnight with gentle agitation. A second aliquot of BTFMA was added and incubated for 6 h before the resin was loaded onto a gravity column. The resin was washed with 4 bed-volumes of wash buffer (50 mM HEPES, pH 7.4, 300 mM NaCl, 0.05% LMNG, and 20 mM imidazole), and A_{2A}R was eluted with 50 mM HEPES, pH 7.4, 300 mM NaCl, 0.05% LMNG, and 250 mM imidazole. Eluted receptors were exchanged to LMNG storage buffer (50 mM HEPES, pH 7.4, 300 mM NaCl, 0.05% LMNG), then incubated with XAC-agarose gel (Affi-Gel 10 conjugated with A_{2A}R antagonist xanthine amine congener) at 4°C overnight with gentle agitation (Weiss and Grisshammer, 2002).

A_{2A}R-bound XAC resin was loaded onto a gravity column, washed with 2 bed-volumes of LMNG storage buffer (50 mM HEPES, pH 7.4, 300 mM NaCl, 0.05% LMNG) followed by 1 bed-volume of cholate buffer (50 mM HEPES, pH 7.4, 100 mM NaCl, 15 mM sodium cholate). A_{2A}R was eluted with 50 mM HEPES, pH 7.4, 100 mM NaCl, 15 mM sodium cholate, and 30 mM theophylline, then exchanged to cholate buffer prior to nanodisc assembly.

Nanodisc assembly and purification

Cholate-solubilized lipid, A_{2A}R, and MSPΔH5 (Hagn et al., 2013) (produced in-house) were mixed in HNE buffer (20 mM HEPES, pH 8.0, 100 mM NaCl, 0.5 mM EDTA) with a final concentration of 15 mM cholate, 3.5 mM lipid, and 100 μM MSPΔH5. The lipid mixture contained a 3:2 ratio of 1-palmitoyl-2-oleoyl-sn-glycero-3-phosphocholine (POPC) to 1-palmitoyl-2-oleoyl-sn-glycero-3-phospho-(1'-rac-glycerol) (POPG). A minimum 10-to-1 MSPΔH5:A_{2A}R ratio was employed to ensure each nanodisc contains only one receptor. Empty nanodiscs were prepared using the identical procedure without including A_{2A}R. The mixture was incubated on ice for 1 h, followed by the addition of 0.6 g/mL Bio-Beads SM-2 resin (BioRad) and an additional 5 h incubation at 4°C with gentle agitation. Bio-Beads were removed using a gravity column, and the assembled nanodiscs were purified on a HiLoad 16/600 Superdex 200 prep grade size exclusion column equilibrated with nanodisc storage buffer (50 mM HEPES, pH 7.4, 100 mM NaCl) at a flow rate of 1 mL/min. Monomeric nanodiscs eluted at around 65 mL (Figure S1). The peak was pooled, incubated with TALON resin for 2 h at 4°C, then washed extensively with nanodisc storage buffer to remove empty nanodiscs. A_{2A}R-containing nanodiscs were eluted with 50 mM HEPES, pH 7.4, 100 mM NaCl, and 250 mM imidazole, then concentrated and buffer-exchanged to nanodisc storage buffer for downstream experiments.

$G_s\alpha$ expression and purification

A pET15b plasmid containing a modified GNAS2 gene immediately downstream of an open reading frame for His_6-tagged maltose binding protein (MBP) and TEV cleavage site was the generous gift from Dr. Oliver Ernst at the University of Toronto. This short isoform of human $G_s\alpha$ was originally designed for the purpose of chemoselective labeling and harbors the Y358C mutation along with all other solvent-exposed cysteines replaced (C3S, C200T, C237S, C359I, C365A, C379V). Analogous mutants have previously been made for $G_i\alpha$, and have been shown to retained native-like fold and function (Kaya et al., 2014; Medkova et al., 2002). The plasmid was transformed into *Escherichia coli* (*E. coli*) BL21 (DE3) cells by heat shock and screened on agar plates containing 100 μg/mL ampicillin. A single colony was grown in 10 mL of LB medium (0.5% yeast extract, 1% tryptone, 1% NaCl, 100 μg/mL ampicillin) overnight at 37°C with shaking. This starter culture was inoculated into 1 L of LB medium with ampicillin and grown at 25°C with shaking to an optical density at 600 nm (OD_{600}) of 0.3. Cells were grown for an addition hour at 19°C, then induced with isopropyl β-d-1-thio-galactopyranoside (IPTG) to a final concentration of 50 μM. After overnight induction, cells were harvested by centrifugation at 6,000 g for 10 min.

Cell pellets were resuspended in ice-cold lysis buffer (50 mM sodium phosphate, pH 8.0, 300 mM NaCl, 10 mM imidazole, 50 μM GDP, 2 mM $MgCl_2$, 0.5 mM TCEP, 5 mM 6-aminocaproic acid, 5 mM benzamidine, 0.4 mg/mL lysozyme, 2 μg/mL DNase I, 10% glycerol) and lysed by sonication. The lysate was centrifuged at 8,000 g for 2 h, and the resulting supernatant was incubated with Ni-NTA resin for 3 h at 4°C with gentle mixing. The resin was washed with 4 bed-volumes of lysis buffer containing 20 mM imidazole, then eluted with 50 mM sodium phosphate (pH 8.0), 100 mM NaCl, 50 μM GDP, 2 mM $MgCl_2$, 0.5 mM TCEP, 10% glycerol, and 250 mM imidazole. The eluted MBP-$G_s\alpha$ fusion protein was buffer exchanged to remove imidazole, then incubated with 10 μg/mL of TEV protease (produced in-house) overnight at 4°C without agitation. The sample was loaded onto a Ni-NTA column, and the flow-through containing $G_s\alpha$ without an N-terminal MBP was purified on a HiLoad 16/600 Superdex 200 prep grade size exclusion column equilibrated with 50 mM HEPES, pH 7.4, 100 mM NaCl, 2 mM $MgCl_2$, 5 μM GDP, and 10% glycerol at a flow rate of 1 mL/min. $G_{\alpha s}$ eluted at around 80 mL (Figure S2). The peak was pooled, concentrated, and GDP was added to a final concentration of 100 μM for downstream experiments.

Mini-$G_s\alpha$ expression and purification

A pET15b plasmid containing a modified mini-$G_s\alpha$ gene (Carpenter et al., 2016) immediately downstream of an open reading frame for a His_6 tag and TEV cleavage site was gifted by Dr. Oliver Ernst at the University of Toronto. Like $G_s\alpha$ above, this protein was originally designed for the purpose of chemoselective labeling and harbors the Y358C mutation along with all other solvent-exposed cysteines replaced (C237S, C359I, C365V, C379V; amino acid number aligned with that of $G_s\alpha$). The plasmid was transformed into *E. coli* BL21 (DE3) cells by heat shock and screened on agar plates containing 100 μg/mL ampicillin. A single colony was grown in 10 mL of LB medium (0.5% yeast extract, 1% tryptone, 1% NaCl, 100 μg/mL ampicillin) overnight at 37°C with shaking. This starter culture was

inoculated into 1 L of LB medium with ampicillin and grown at 37°C until an OD_{600} of 0.6. Cells were induced overnight at 25°C with 100 μM IPTG and harvested by centrifugation at 6,000 g for 10 min. Mini-$G_s\alpha$ was purified using identical protocol as $G_s\alpha$, with the exception that the final size-exclusion chromatography step was omitted. The purified protein was buffer exchanged to 50 mM HEPES, pH 7.4, 100 mM NaCl, 2 mM $MgCl_2$, 100 μM GDP, and 10% glycerol for downstream experiments.

Gβγ expression and purification

Spodoptera frugiperda Sf9 cells were grown in I-Max insect cell culture medium (Wisent Inc.) to a density of 2 million cells/ml (≥98% viability) and then co-infected with two separate *Autographa californica* nuclear polyhedrosis viruses, one harboring the gene for His_6-human $G\beta_1$ (GNB1) and human $G\gamma_2$ (GNG2), and the other harboring the gene for human $G_i\alpha$, to produce Gβγ complex for experiments. Multiplicity of infection (MOI) of 0.75 (Gβγ) and 1.0 ($G_i\alpha$) were used for viral infection. The infected cells were grown at 27°C for 48-58 h before harvesting at 1000 g for 20 mins.

Cell pellets were resuspended in ice-cold lysis buffer (50 mM HEPES, pH 8.0, 65 mM NaCl, 2 mM $MgCl_2$, 20 μM GDP, 5 mM 6-aminocaproic acid, 5 mM benzamidine, 5 mM β-mercaptoethanol, 1 μg/mL DNase I) and lysed using a microfluidizer at 2,000 psi in 1 pass. The lysate was centrifuged at 1,000 g for 10 min and the resulting supernatant was centrifuged at 100,000 g for 90 min. Pellets from the ultracentrifugation was resuspended in membrane wash buffer (50 mM HEPES, pH 8.0, 50 mM NaCl, 5 mM $MgCl_2$, 20 μM GDP, 5 mM 6-aminocaproic acid, 5 mM benzamidine, 5 mM β-mercaptoethanol), centrifuged again at 100,000 g for 90 min, then resuspended in membrane wash buffer containing 2% sodium cholate. The resuspended membrane was solubilized for 1 h at 4°C prior to centrifugation at 100,000 g for 30 min. The resulting supernatant was collected, and detergent was exchanged by slowly adding a five-fold volume of dilution buffer (20 mM HEPES, pH 8.0, 200 mM NaCl, 5 mM $MgCl_2$, 10 mM imidazole, 0.05% n-dodecyl β-D-maltoside (DDM), 30 μM $AlCl_3$, 5 mM NaF, 20 μM GDP, 1 mM DTT) over a 1 h period. The sample was incubated with Ni-NTA resin for 2 h at 4°C with gentle mixing. The resin was washed extensively with wash buffer (20 mM HEPES, pH 8.0, 40 mM NaCl, 5 mM $MgCl_2$, 10 mM imidazole, 30 μM $AlCl_3$, 5 mM NaF, 0.05% DDM, 20 μM GDP, 5 mM β-mercaptoethanol) prior to elution with 250 mM imidazole. The eluted protein was loaded onto a Macro-Prep High Q anion exchange column (Bio-Rad) equilibrated with buffer A (20 mM HEPES, pH 8.0, 40 mM NaCl, 2 mM $MgCl_2$, 0.025% DDM, 20 μM GDP, 200 μM TCEP), washed extensively with 5% buffer B (buffer A with 1 M NaCl), then eluted with a gradient of 6%–40% buffer B. Fractions containing Gβγ (~24% buffer B, Figure S2) were pooled and exchanged to final storage buffer (50 mM HEPES, pH 7.4, 100 mM NaCl, 2 mM $MgCl_2$, 0.0125% DDM, 100 μM TCEP, 100 μM GDP, 10% glycerol) for downstream experiments.

NMR experiments

NMR samples were prepared in either nanodisc storage buffer or G protein storage buffer (when Gα or Gαβγ were present) with 20-100 μM BTFMA-labeled A_{2A}R-V229C, 20 μM sodium trifluoroacetate (TFA) as the ^{19}F chemical shift reference, and 10% D_2O. When applicable, samples also contained a 5-fold excess of Gα (relative to A_{2A}R) or 1.2-fold excess of Gαβγ, and saturating concentrations of A_{2A}R ligands (2 mM NECA, 500 μM LUF5834, or 500 μM ZM241385). All samples were sterile-filtered and prepared in sterile Shigemi tubes to prevent microbial contamination. NMR experiments were acquired at 20°C on a 600 MHz Varian Inova spectrometer equipped with a triple-resonance cryoprobe tunable to ^{19}F. A typical fluorine NMR experiment included a 300 ms recycle delay, a 7 μs (45°) excitation pulse, and a 600 ms acquisition time. Spectra were acquired using 50,000-200,000 scans, yielding a S/N of approximately 50-100. Spectra were processed using MestReNova (Mestrelab Research S.L.) employing chemical shift referencing (−75.6 ppm for TFA), baseline correction, zero filling, and exponential apodization equivalent to a 20 Hz line broadening. The transverse relaxation time (T_2) of ^{19}F-labeled A_{2A}R-V229C saturated with agonist (NECA) was measured using a CPMG T_2 pulse sequence, using a refocusing period of 120 μs and total transverse magnetization evolution times of 0.48, 0.96, 1.44, 1.92, 2.4, 2.88, 3.36, 3.84, 4.32, 4.8, and 6.24 ms. Peak intensities from spectra in the T_2 series were fit to exponential decay functions ($I_t = I_0 e^{-t/T_2}$) (Figure S3). To the extent that the resonances could be resolved, T_2 relaxation measurements provided an estimate of the homogeneous contribution to linewidth ($\Delta\nu_{1/2}^{homo} = 1/\pi T_2$).

NMR spectral deconvolution

Spectral deconvolutions were performed using MestReNova assuming generalized Lorentzian line shapes, characterized by a frequency, ν_i, intensity, I_i, width at half-height, $\Delta\nu_{1/2,i}$, and a kurtosis parameter in the range of −1 to 1. As discussed below, it was possible to define the activation ensemble in terms of three resonances, A_1-A_3, whose frequencies ($\nu_1 - \nu_3$) could be globally fitted from the entire spectral series as a function of ligand, GDP-bound G protein, and nucleotide-free G protein. In some cases, exchange broadening and/or coalescence suggested very slight deviations in these resonances (*e.g.* a slight coalescence of A_1 and A_2 in the case of the NECA + G protein spectra). In general, chemical shift values for A_1, A_2, and A_3 were allowed to vary by no more than 0.03 ppm. To assess the uncertainty in peak fitting and to ensure deconvolution is robust against spectral noise, three additional spectra were acquired under identical conditions but in the absence of A_{2A}R. The noise spectra were then added to the nine parent spectra shown in Figure 3, generating three additional noise-added spectra for each condition. Deconvolutions were performed again for each of the noise-added spectra while holding the chemical shifts and kurtosis factors constant to determine variations in intensity of the deconvolved peaks and sensitivity of deconvolved peak intensities to noise. Peaks from all four spectral fittings (parent + three noise-added) were used to calculate the mean and standard deviation of the percent populations presented in Figures S4 and S7.

NMR spectral assignments and validation of chemical shifts

Building on our earlier ^{19}F NMR study of A_{2A}R-V229C in detergent micelles (Ye et al., 2016), the ^{19}F NMR spectra in nanodiscs exhibit a clear downfield resonance whose intensity decreases with the addition of agonist and/or G protein. The chemical shift of this inactive state, designated as $S_{1\text{-}2}$, was also observed to vary in accordance with the hypothesis that there is an equilibrium between two unique inactive states (*i.e.* ionic lock "on" or S_1 and ionic lock "off" or S_2) which undergo mutual millisecond timescale exchange, resulting in some weighted average of the two ($S_{1\text{-}2}$). In nanodiscs, the spectral series suggests that S_1 and S_2 states exchange on an intermediate or slow timescale, relative to that observed earlier in micelles. Upon saturation of the receptor by agonist the intensity of the inactive signature decreases while the inactive state resonance is observed to shift downfield, suggesting the equilibrium has shifted to the ionic lock "off" state for the inactive conformers remaining in the ensemble. In addition to the above inactive state resonance, all of the ^{19}F NMR spectra (*i.e.* as a function of ligand, G protein, and nucleotide) exhibit multiple upfield resonances characteristic of the active ensemble states. Three active states (A_1, A_2, A_3) were assigned from a global analysis of all nine spectra in Figures 3B–3D by first identifying common local maxima and inflection points. The location of the A_1 resonance was identified in the receptor + full agonist spectrum (without G protein, dark green trace in Figure 3D). This state is also partially resolved in the receptor + partial agonist + nucleotide-free G protein spectrum (light blue trace in Figure 3C) and appears as a shoulder in the spectra of the apo receptor + G protein both with and without GDP (dark gray and light gray traces in Figure 3B). A_2 is assigned from the fully resolved peak in the receptor + partial agonist + nucleotide-free G protein spectrum (light blue trace in Figure 3C), as well as the apo receptor spectrum in the presence of G protein (dark gray trace in Figure 3B). Similarly, A_3 was assigned from the maxima observed in the dark gray trace in Figure 3B, the shoulder in the light blue trace in Figure 3C, and the shoulder in the middle green trace in Figure 3D.

To further validate the assigned chemical shifts, we performed non-linear least-squares curve fitting for each spectrum (from −59 ppm to −64 ppm) using the MATLAB built-in function lsqcurvefit. Here, each NMR profile was modeled as a sum of four Lorentzian lines (one corresponding to the inactive resonance and three corresponding to the active resonances). An initial guess for each parameter (ν_i, I_i, and $\Delta\nu_{1/2,i}$), based on spectral deconvolutions performed in MestReNova (described above), was supplied and when applicable, boundaries for line widths and intensities were specified. After fixing the parameters associated with the inactive resonance, lsqcurvefit was tasked to find the optimal frequency, intensity, and width associated with each active resonance while minimizing the sum of squared residuals. A summary of the analysis is provided below.

Beginning with the spectra of A_{2A}R with saturating concentrations of agonist, NECA (Figure S5A), it is clearly possible in this case to fit the active state resonances to two Lorentzian lines as shown. However, as discussed in Figure S3 and the main text, the deconvolved line widths associated with the A_2 resonance disagree with that estimated from T_2 measurements by a factor of ~2.5. After imposing an upper limit on the line widths of 140-170 Hz (accounting for line broadening from exponential apodization) for A_1 and A_2, the resulting fit recapitulates the two maxima but does not capture the upfield signal in the deconvolution. In comparison, a three-state activation ensemble, being the next simplest possible model, produces a better fit. The third Lorentzian line, A_3, was found to be a broad resonance in the absence of G protein.

We next consider the apo receptor spectra as shown in Figure S5B, where all three spectra are deconvolved assuming the active ensemble is represented by the identical three states, A_1, A_2, and A_3, defined above. Beginning with the spectrum associated with GDP-loaded G protein bound to the apo receptor, we can distinguish all three active state resonances as local maxima, without any adjustment to the fitted frequencies, ν_1, ν_2, or ν_3. Upon removal of GDP, these same frequencies appear to persist in the deconvolution in the topmost spectrum. In the absence of either G protein or ligand, however, the active ensemble is characterized by significant exchange broadening and we assume that the identical resonances are present, albeit broadened.

The NECA (full agonist) series of spectra, shown in Figure S5C, reveal a similar story. Again, the addition of GDP-bound G protein results in a well-defined A_3 resonance, although A_1 and A_2 cannot be deconvolved with confidence due to apparent coalescence of the two resonances and exchange broadening. The identical frequencies, ν_1, ν_2, and ν_3, used in the global analysis, are nevertheless shown as a reference. Finally, the partial agonist series of spectra, shown in Figure S5D, suggest the identical 3 resonances are again present in the nucleotide-free spectrum (topmost) while excessive exchange broadening and coalescence in the other two spectra make them difficult to be definitively deconvolved.

Deconvolutions of all nine spectra reveal some interesting observations: 1) a three-state active ensemble model (A_1, A_2, A_3) is necessary. Following the principle of Occam's razor, this is the simplest model if we are to take into account T_2 relaxation measurements, 2) in the absence of G protein, the A_3 resonance is characteristically broad for apo, NECA- and LUF-bound receptor, in keeping with the idea that the precoupled state is dynamic and samples a broad range of local sub-states, perhaps to facilitate binding to G protein, and 3) while there is a modest degree of exchange broadening and coalescence in a few of the spectra, the global assignment of the three frequencies, ν_1, ν_2, and ν_3, agrees well with the spectra without the need for any adjustments in the frequencies.

GTP hydrolysis experiments

The GTP hydrolysis experiments were performed using the Promega GTPase-Glo™ assay kit following the manufacturer's protocol (Mondal et al., 2015). Briefly, Gα or Gαβγ were incubated with A_{2A}R or empty nanodiscs at room temperature in G protein storage buffer containing 1 μM GDP, 4 μM GTP, and 25 μM A_{2A}R ligand (when applicable), at a final concentration of 250 nM G protein, 250 nM, 500 nM, or 1000 nM A_{2A}R, and 250 nM empty nanodiscs. Control reactions consist of identical buffer solutions with GTP but in the absence of either A_{2A}R, G protein, or both. After 90 min, unreacted GTP was converted to ATP through the addition of a GTPase-Glo reagent. Subsequently, detection reagent containing luciferase was added and the resulting luminescence was

measured using a TECAN Spark multi-mode plate reader with an integration time of 1 min. The luminescence signal intensity is directly proportional to the amount of unreacted GTP. Therefore, GTP hydrolysis can be calculated for the following:

In the absence of $A_{2A}R$:

$$\Delta Lum_G = Lum(\text{buffer only}) - Lum(\text{G protein only})$$

In the presence of $A_{2A}R$:

$$\Delta Lum_{G+R} = Lum(\text{buffer with } A_{2A}R \text{ but no G protein}) - Lum(\text{G protein} + A_{2A}R)$$

where Lum = luminescence signal intensity

The increase in GTP hydrolysis as a result of increased nucleotide exchange mediated by $A_{2A}R$ (Figure 4 in the main text) was calculated as follows:

$$\%\ \text{Increase GTP hydrolysis} = \frac{\Delta Lum_{G+R} - \Delta Lum_G}{\Delta Lum_G} \times 100$$

Native-PAGE

$A_{2A}R$ (20 μM) was combined with equimolar Gα or Gαβγ in G protein storage buffer containing 500 μM $A_{2A}R$ ligand (when applicable). Loading buffer was added (final concentration of 50 mM Tris-HCl, pH 7.0, 20% glycerol, and 0.01% bromophenol blue) and the samples were resolved on a 4%–15% tris-glycine polyacrylamide gel (BioRad) at 100 V for 2 h. The gel was stained with Coomassie brilliant blue.

SPR experiments

SPR experiments were performed in triplicates using a benchtop OpenSPR instrument (Nicoya) equipped with a gold nanoparticle sensor chip conjugated with Ni-NTA. All experiments were performed under constant flow (40 μL/min G protein storage buffer containing 20 μM GDP and 100 μM NECA or LUF5834) over a sensor chip saturated with nanodisc-stabilized $A_{2A}R$, which was immobilized to the chip via the C-terminal histidine tag. After a stable baseline was reached, Gαβγ was injected at three different concentrations (30 nM, 90 nM, and 270 nM) and allowed to interact with the $A_{2A}R$-bound sensor chip until maximum dissociation was observed. Binding curves obtained at the three concentrations were simultaneously fit to a one-to-one binding model using TraceDrawer (Ridgeview Instruments). We note that in our system, incomplete dissociation was observed which was likely a result of a small fraction of Gβγ inserting into the nanodiscs (due to the isoprenyl lipid anchor on the γ subunit). Therefore, the last segment of the dissociation phase was excluded in the analysis of the binding curves. This was possible since the minimum amount of dissociation needed for an accurate off rate calculation is 5%.

$A_{2A}R$-Gαβγ modeling

The wild-type $A_{2A}R$ bound to NECA and mini-$G_s\alpha$ (based on the PDB structure 5G53 (Carpenter et al., 2016)) was first relaxed by MD simulations in 4:1 POPC:cholesterol (CHL) membranes. The relaxed structure was used as starting point to construct the fully active state of $A_{2A}R$ in complex with wild-type $G_s\alpha\beta\gamma$. The relaxation procedure of the $A_{2A}R$/NECA/mini-G complex was as follows: The missing intracellular loop 3 connecting TM5 and TM6 was modeled using the MODELER package. After energy minimization and equilibration, 3 successive iterations of 1 μs leap-frog integration MD simulations were conducted, assuming an isothermal-isobaric ensemble using a Nose-Hoover thermostat (Hoover, 1985; Nosé, 1984) and a Parrinello-Rahman barostat (Parrinello and Rahman, 1981) to mimic 300 K and 1 bar conditions. We carried out carbon-α clustering for the last 500 ns of simulation using a GROMOS clustering algorithm (Daura et al., 1999) to obtain the highest populated structure before proceeding to the next step. The construction of the $A_{2A}R$/NECA/G_s complex was as follows: The Gα subunit was homology modeled using the mini-G structure while the missing regions in the nucleotide binding pocket and the remainder of G_s were modeled based on the structure of the GDP-bound G_s heterotrimer (PDB: 6EG8 (Liu et al., 2019)). The $A_{2A}R$-$G_s\alpha\beta\gamma$ complex was then inserted into the POPC-4:1-CHL extended membrane, equilibrated and relaxed in a 1 μs simulation. An AMBER 14SB forcefield (Maier et al., 2015) was used to represent the intramolecular interactions of protein, and a GAFF forcefield (Wang et al., 2004) was introduced for NECA and GDP. All the simulation boxes were solvated using a TIP3P water model (Jorgensen et al., 1983), while maintaining a 0.15 M NaCl concentration.

Allostery computations using rigidity transmission theory

To probe allosteric communication in the $A_{2A}R$-heterotrimeric G protein complex, we utilized the rigidity-transmission allostery (RTA) algorithm, whose details have been previously described (Ye et al., 2018). The RTA algorithm is a computational method based on mathematical rigidity theory (Whiteley, 2005), which predicts how perturbations of conformational rigidity and flexibility (conformational degrees of freedom) at one site transmit across a protein structure to modify degrees of freedom at other distant sites. Here, RTA was applied to examine the allosteric pathways between the orthosteric pocket of the receptor and distal regions in the $A_{2A}R$-Gαβγ complex with a focus on the GDP pocket and Gβγ.

Starting with the model of NECA-bound $A_{2A}R$ complexed with GDP-bound heterotrimer, a constrained network representation of protein structure was generated with the method FIRST (Floppy Inclusions and Rigid Substructure Topography (Jacobs et al., 2001))-an initial step in the RTA method. The constrained network consists of nodes (atoms) and edges representing covalent and non-covalent interactions (*i.e*. covalent bonds, hydrogen bonds, hydrophobic interactions etc.). Hydrogen bonds are ranked in terms of overall strength, whereupon a hydrogen bond energy cut-off value is selected such that all bonds weaker than this cut-off are ignored. The pebble game algorithm (a component of FIRST software) was used to quantify rigidity and flexibility and evaluate available conformational degrees of freedom throughout the constrained network. We then applied the RTA algorithm to quantify the available conformational degrees of freedom at every window of three consecutive residues (*i.e*. a sliding window filter along the length of the receptor) before and after perturbation of rigidity at the orthosteric pocket (NECA). The extent of the ''degree of freedom transmission'' was then extracted for each residue. This process was repeated by successively ignoring weak hydrogen bonds in small steps of 0.01 kcal/mol. Each residue was then assigned the allosteric intensity response by averaging the total degree of freedom transmission as a function of energy cut-off using three neighboring windows containing that residue. Residues with high allosteric intensity transmission define the allosteric pathway connecting the orthosteric pocket and distant residues in the receptor and $G_s\alpha\beta\gamma$. To visualize results, residues are colored on the structure based on the amount of allosteric transmission.

QUANTIFICATION AND STATISTICAL ANALYSIS

Each NMR spectrum was acquired using 1-2 freshly prepared sample(s) and a cumulative 50,000 to 200,000 scans until sufficient S/N was achieved. Experiments were monitored to ensure that the peak shapes do not change over time and that the sample remains stable throughout the experiment. Each experimental series were performed on the same batch of receptors (i.e., all spectra in Figure 1 were acquired using receptors from the same cell pellet, purified as a single batch. Same goes for Figure 3). Statistical analysis was performed in either Microsoft Excel (Figures 5, S3, and S7) or GraphPad Prism 8.4.2 (Figure 4). Statistical details can be found in figure legends where applicable. Briefly, GTP hydrolysis data were presented as mean ± SEM ($n \geq 3$). In Figure 4A, statistical significance was determined by either a two-way ANOVA followed by the Bonferroni (comparison of $G\alpha$ and $G\alpha\beta\gamma$ for each ligand) or the Tukey test (comparison of each ligand condition to each other). In Figure 4B, statistical significance was determined a multiple t test using the Holm-Sidak method. In all cases, * $p \leq 0.05$; ** $p \leq 0.01$; *** $p \leq 0.001$; **** $p \leq 0.0001$. Kinetic parameters derived from SPR data represent mean ± SD ($n = 3$, Figure 5). Given that the uncertainties between trials are much larger than the fitting error of the binding curves within each trial, the former is presented. In estimating percent population of states from deconvolution of NMR spectra (Figure S7), data represent mean ± SD from four individual fits. In each case, three noise spectra (of equivalent noise amplitude to that of the baseline in the original spectrum) were added to the original spectrum, generating three new daughter spectra. All 4 spectra were then deconvolved and the intensities were allowed to vary in each fit. For additional details see the STAR Methods section.

CellPress

Supplemental figures

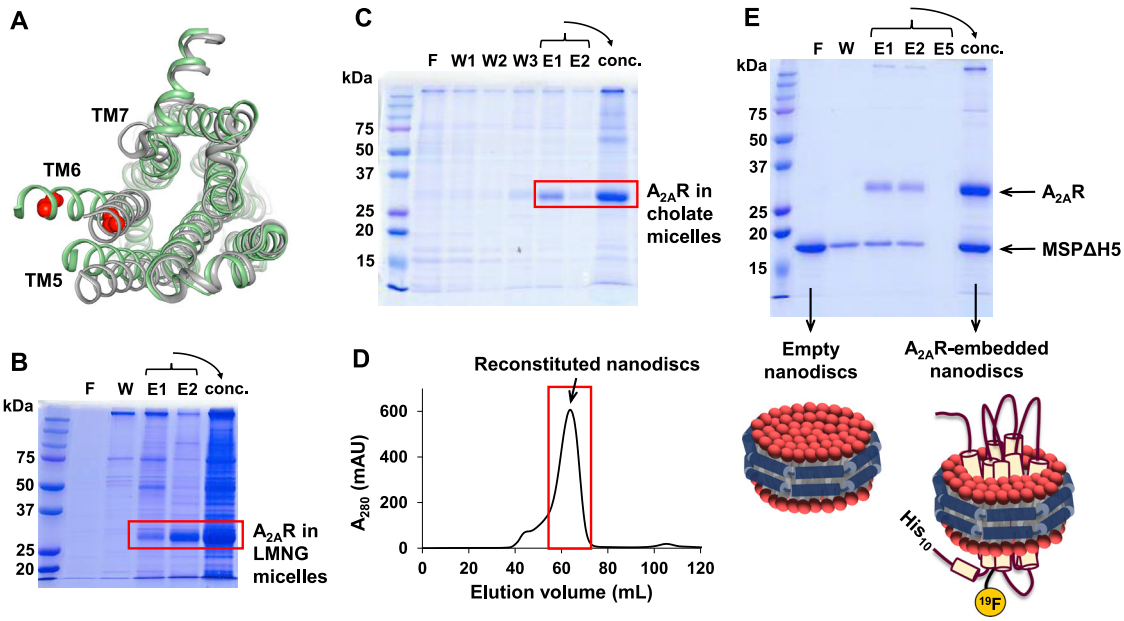

Figure S1. ^{19}F-labeling site and receptor purification, related to STAR Methods

(A) Overlay of the inactive (gray, PDB: 4EIY; Liu et al., 2012) and active (green, PDB: 5G53 (Carpenter et al., 2016)) crystal structures of $A_{2A}R$ viewed from the intracellular side with V229C$^{6.31}$ shown as red spheres. Upon activation, TM6 adopts an outward orientation accompanied by movements in TM5 and TM7. The ^{19}F probe is positioned to detect conformational and environmental changes at the intracellular milieu with high chemical shift sensitivity (Ye et al., 2016). **(B-E)** Purification of $A_{2A}R$-V229C monitored by SDS-PAGE after elution from the metal affinity column (**B**), the XAC ligand affinity column (**C**), and size exclusion column following nanodisc reconstitution (**D**). A monodisperse peak was pooled (red box, (**D**) and further purified via metal affinity chromatography (**E**), which separated empty nanodiscs and those containing $A_{2A}R$. F, flow-through; W, wash; E, elution; conc, elution fractions pooled and concentrated.

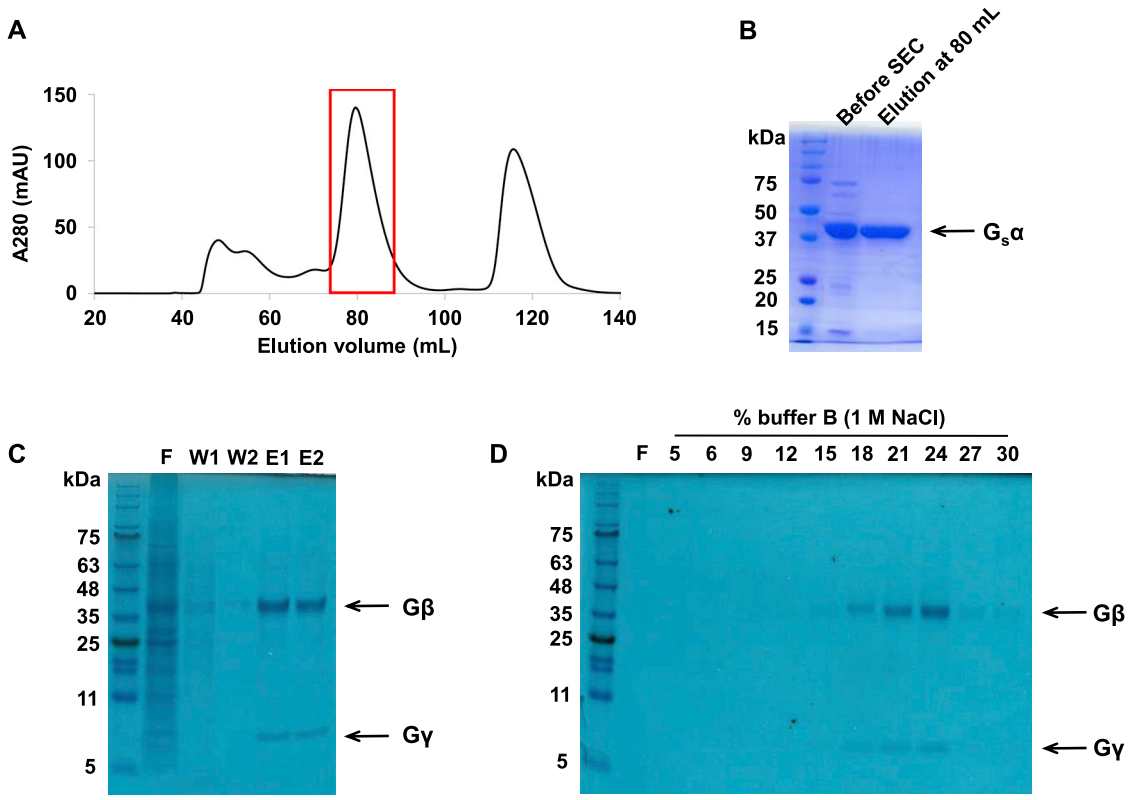

Figure S2. G protein purification, related to STAR Methods

(A) Size exclusion chromatogram of $G_s\alpha$-Y358C. The peak around 80 mL (red box) was collected. (**B**) Gel from SDS-PAGE showing Gα before purification by size-exclusion column and the final product. **(C-D)** Purification of Gβγ monitored by SDS-PAGE. The heterodimer was isolated from cell lysate via metal affinity chromatography (C), then further purified through an anion exchange column (D). F, flow-through; W, wash; E, elution.

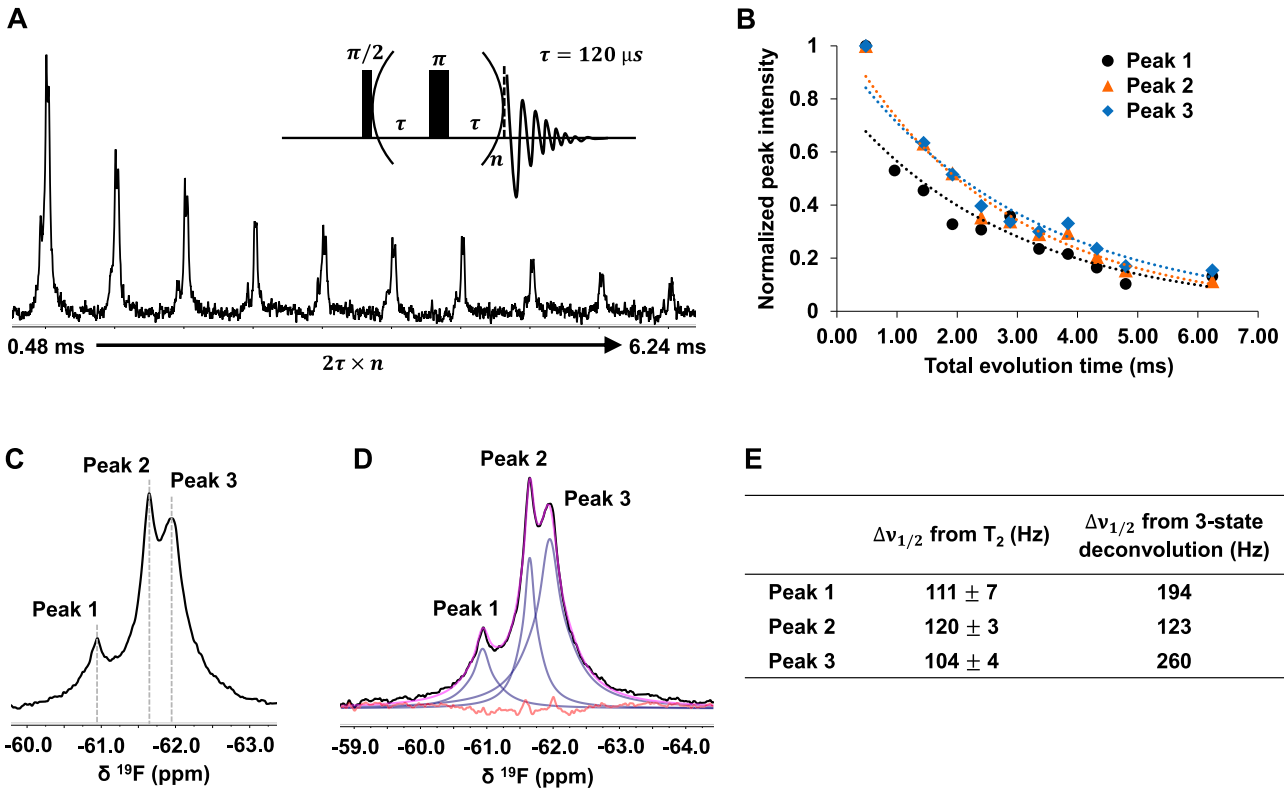

	$\Delta\nu_{1/2}$ from T_2 (Hz)	$\Delta\nu_{1/2}$ from 3-state deconvolution (Hz)
Peak 1	111 ± 7	194
Peak 2	120 ± 3	123
Peak 3	104 ± 4	260

Figure S3. NMR line widths predicted from T_2 relaxation measurements do not support a 3-state deconvolution of the experimental spectra, related to Figure 1

(A) ^{19}F NMR spectra of NECA-bound A_{2A}R-V229C recorded in a T_2 relaxation experiment (pulse sequence shown in inset). (B) Exponential fit of peak intensities from the T_2 relaxation series for peaks indicated in C. (D) Three-state deconvolution of the spectrum shown in C at indicated chemical shifts (dotted gray lines). Fitted peaks: navy; sum of fitted peaks: magenta; original spectrum: black; residual fitting error: red. (E) Values of the natural linewidths ($\Delta\nu_{1/2}$) derived from T_2 measurements and those predicted by a 3-state spectral deconvolution. Line width uncertainties were obtained from linear regressions of the *ln*(normalized peak intensity) versus time plots (linearizing curves in B).

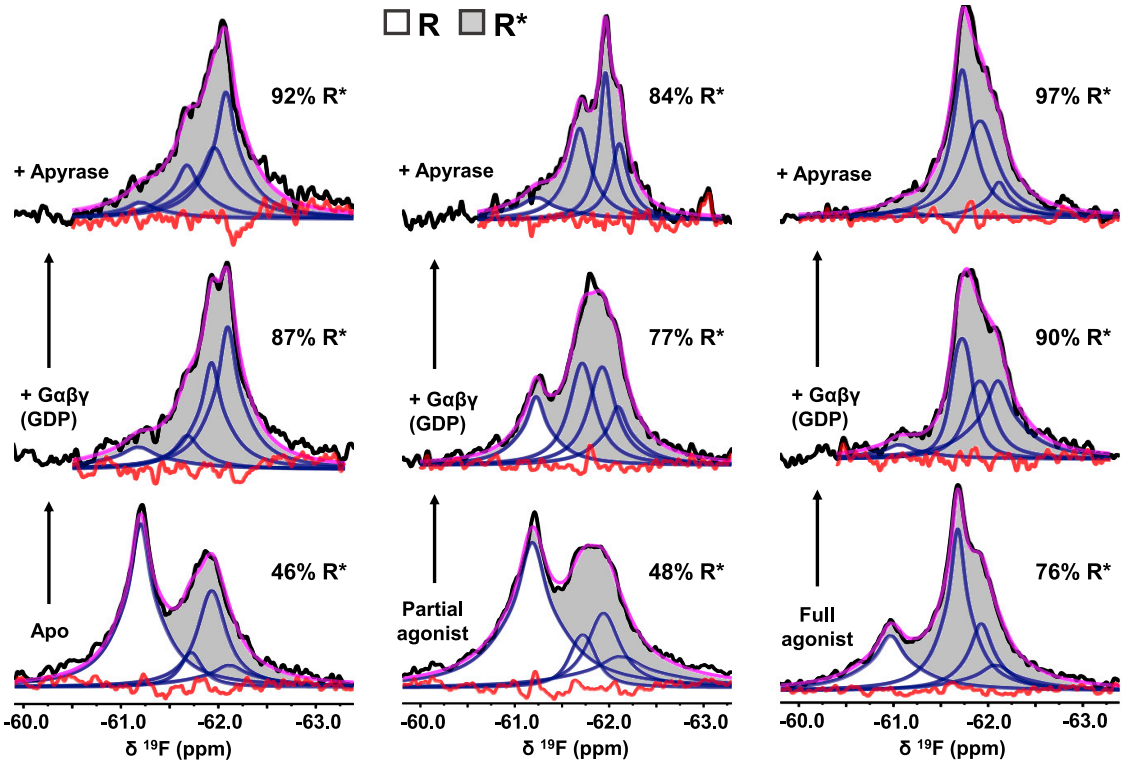

Figure S4. Relative fractions of R* do not correlate directly with receptor GEF activity, related to Figure 3

Spectral deconvolutions of representative ^{19}F NMR spectra considering an inactive ensemble (R, white regions) and an active ensemble (R*, gray regions) containing three active state conformers at $A_1 = -61.70 \pm 0.03$ ppm, $A_2 = -61.95 \pm 0.03$ ppm, and $A_3 = -62.10 \pm 0.02$ ppm. The percent area of R* is indicated for each condition. Fitted peaks: navy; sum of fitted peaks: magenta; original spectra: black; residuals: red.

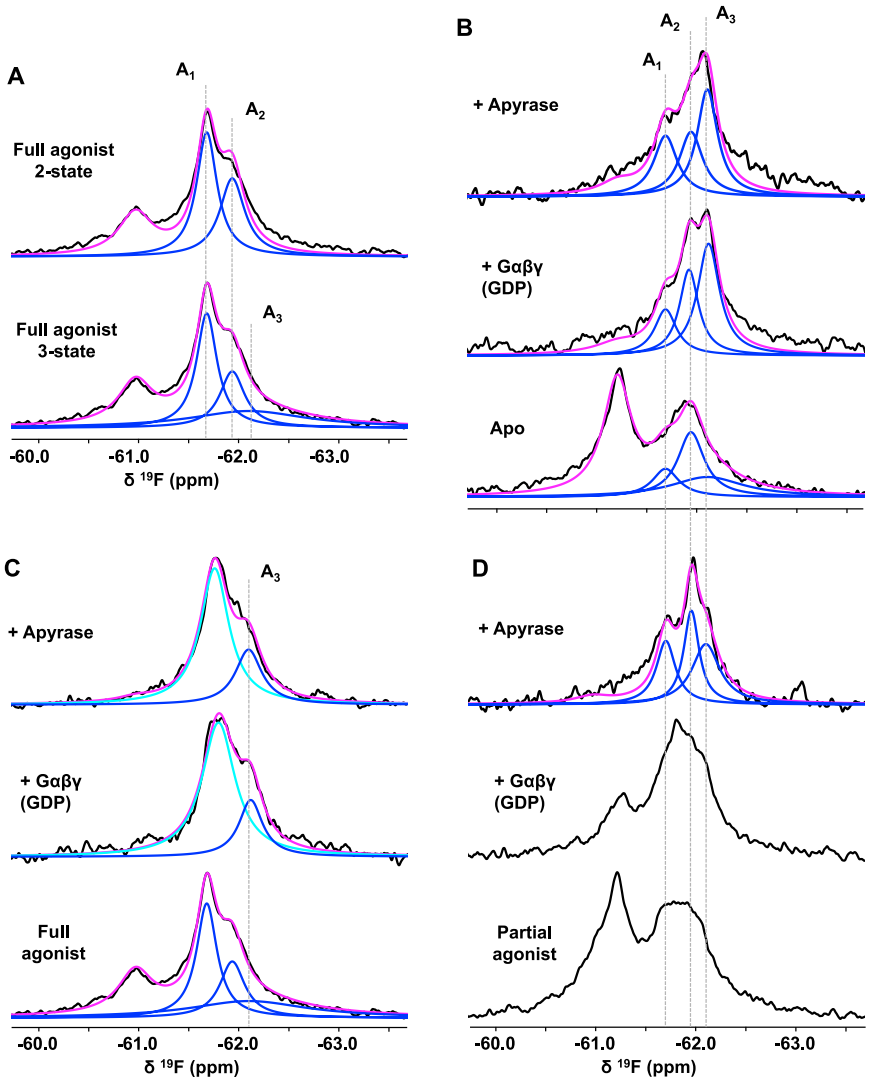

Figure S5. Least-squares curve fitting of the ^{19}F NMR spectra validates a three-state activation model and the associated chemical shifts, related to Figure 3

(A) Deconvolutions of the NECA-bound receptor reveal that a three-state active ensemble is necessary if we are to consider line widths predicted by T_2 relaxation measurements. (B) Deconvolutions of the apo-receptor assuming an active state ensemble characterized by three Lorentzian resonances. Nearly identical frequencies were found when compared to the A_1, A_2, and A_3 states shown in A. (C) Deconvolutions of the agonist-bound receptor, showing the reoccurrence and narrowing of the A_3 state when G protein is present. Peak depicted in cyan represents a coalescence of A_1 and A_2 that could not be robustly deconvolved. (D) Deconvolutions of the partial agonist-bound receptor, where identical frequencies were found for A_1, A_2, and A_3 as those identified in A and B. Fitted peaks: blue (cyan in the case of coalescence); sum of fitted peaks: magenta; original spectra: black.

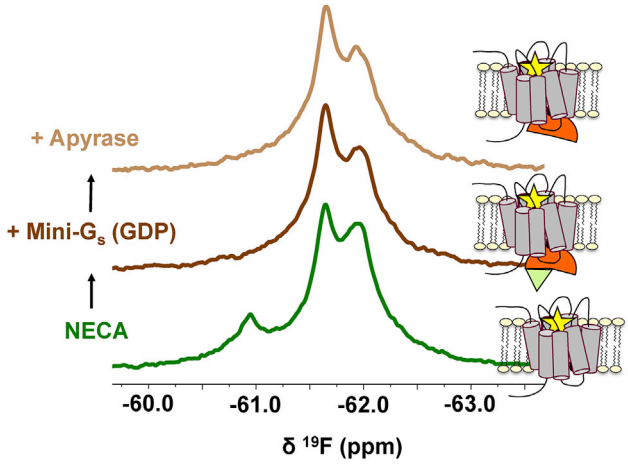

Figure S6. Binding of mini-$G_s\alpha$ promotes the A_1 state, related to Figure 3

^{19}F NMR spectra of agonist-bound $A_{2A}R$ in the presence of an engineered minimal G protein (mini-$G_s\alpha$) with and without GDP.

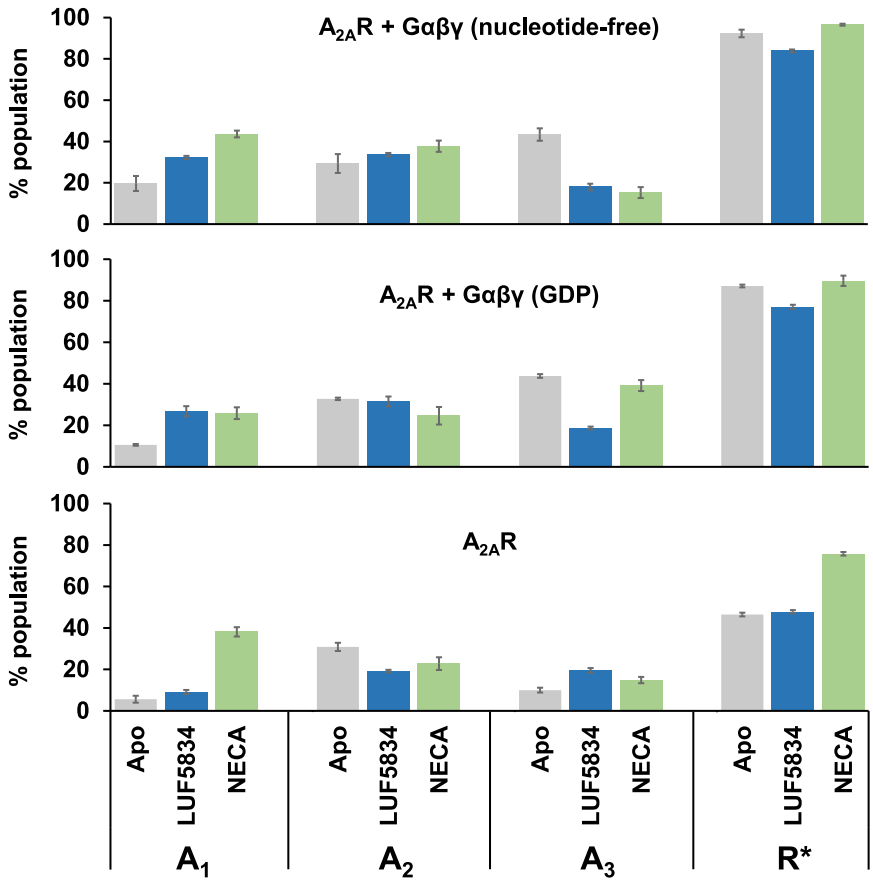

Figure S7. Relative active-state populations of $A_{2A}R$ from NMR spectral deconvolution, related to Figure 3

Percent population of states A_1, A_2, A_3, and R* (summation of all three active states) of $A_{2A}R$ under indicated conditions. Populations are derived from integration of deconvoluted peaks in the ^{19}F NMR spectra shown in Figure S4. Error bars represent standard deviation from four individual fits. In each experimental spectrum, three noise spectra (of equivalent noise amplitude to that of the baseline in the original spectrum) were used to generate three new daughter spectra. All 4 spectra were then deconvolved and the intensities were allowed to vary in each fit. For additional details see the STAR Methods section.